Modeling Nonuniform Thermionic Emission from Heterogeneous Cathodes

By

Dongzheng Chen

A dissertation submitted in partial fulfillment of the requirements for the degree of

Doctor of Philosophy

(Materials Science and Engineering)

at the

UNIVERSITY OF WISCONSIN-MADISON

2022

Date of final oral examination: 05/04/2022

The dissertation is approved by the following members of the Final Oral Committee:
Dane Morgan, Professor, Department of Materials Science and Engineering
John Booske, Professor, Department of Materials Science and Engineering
David Anderson, Professor, Department of Electrical and Computer Engineering
Nader Behdad, Professor, Department of Electrical and Computer Engineering
Ryan Jacobs, Scientist II, Department of Materials Science and Engineering

Acknowledgments

First, I would like to thank my advisors, Professor Dane Morgan and Professor John Booske, for their support and guidance during my PhD studies. They introduced me into the world of vacuum electronics. I would also like to thank Dr. Ryan Jacobs for his mentoring and help on my PhD work.

I am very grateful that I can work with fellow students Dr. Tianyu Ma and Lin Lin. We have been working on this project for multiple years. They have helped me a lot in both my experimental and theoretical studies on this project. I would also like to thank visiting scholar Dr. Qiang Zheng. The discussion broadened my knowledge in thermionic emission and vacuum electronics. I would like to thank Dr. Sariful Sheikh for the valuable discussions on this project.

I would like to thank Professor Yue Ying Lau, Dr. Abhijit Jassem from the University of Michigan, Dr. John Petillo and Dr. David Chernin from Leidos Inc., and Dr. Kevin Jensen for the collaboration on this project. It is my honor to be in a project with collaborators from multiple institutions and have the opportunity to learn from their expertises.

I would like to thank Professor Booske's students Patrick Forbes, Sirous Nourgostar, and Dr. Daniel Enderich. The discussion with them was very helpful for me to get familiar with vacuum electronics. I would also like to thank all other members in Professor Morgan's group and Professor Booske's group for their help during my PhD study.

I would like to thank Dr. Vasilios Vlahos for providing the cathode samples and the heater fixtures, thank Daniel Busbaher from 3M Technical Ceramics for providing the cathodes, thank Professor Martin Kordesch from Ohio University for providing the e-beam heater, and thank Sirous Nourgostar for lending his personal pyrometer to me. Without their help, I cannot finish the experiments of my PhD work.

Finally, I would like to thank my family, friends, coworkers, and my medical team for their help in my life, especially during my darkest days.

This work was funded by the Defense Advanced Research Projects Agency (DARPA) under grant reference number N66001-16-1-4043 through the Innovative Vacuum Electronic Science

and Technology (INVEST) program with Leidos, Inc. I gratefully acknowledge use of facilities and instrumentation supported by NSF through the University of Wisconsin Materials Research Science and Engineering Center (DMR-1720415).

Publications

- Chernin, D., Lau, Y. Y., Petillo, J., Ovtchinnikov, S., <u>Chen, D.</u>, Jassem, A., Jacobs, R., Morgan, D., and Booske, J., 2020. Effect of nonuniform emission on miram curves. *IEEE Transactions on Plasma Science*, 48(1), pp.146-155.
- Chen, D., Jacobs, R., Morgan, D., and Booske, J., 2021. Impact of nonuniform thermionic emission on the transition behavior between temperature-and space-charge-limited emission. *IEEE Transactions on Electron Devices*.
- 3. Chen, D., Jacobs, R., Petillo, J., Vlahos, V., Jensen, K.L., Morgan, D., and Booske, J., 2021. Physics-based model for nonuniform thermionic electron emission from polycrystalline cathodes. Submitted to *Physical Review Applied. arXiv preprint arXiv:2112.02136*.
- 4. <u>Chen, D.</u>, Jacobs, R., Morgan, D., and Booske, J., Physical factors governing the shape of the Miram curve knee in thermionic emission. *arXiv preprint arXiv:2202.08247*.
- 5. Lin, L., Jacobs, R., Ma, T., Chen, D., Booske, J., and Dane Morgan., Work function: Fundamentals, measurement, calculation, engineering, and applications. Submitted to *Physical Review Applied*.
- 6. Lin, L., Jacobs, R., Chen, D., Vlahos, V., Lu-Steffes, O., Alonso, J. A., Morgan, D., and Booske, J., Demonstration of low work function perovskite SrVO₃ using thermionic electron emission. Submitted to *Advanced Functional Materials*.

Conference presentations

All conference presentations listed below are oral presentations.

- Chen, D., Jacobs, R., Vlahos, V., Jensen, K.L., Morgan, D. and Booske, J., 2018. Combining theory and experiment to model electron emission from polycrystalline tungsten cathode surfaces. In 2018 IEEE International Vacuum Electronics Conference (IVEC) (pp. 39-40). IEEE.
- 2. <u>Chen, D.</u>, Jacobs, R., Vlahos, V., Morgan, D. and Booske, J., 2019, April. Statistical model of non-uniform emission from polycrystalline tungsten cathodes. In *2019 International Vac- uum Electronics Conference (IVEC)* (pp. 1-2). IEEE.
- 3. Chen, D., Jacobs, R., Vlahos, V., Morgan, D. and Booske, J., 2019. Modeling spatially heterogeneous electron emission from tungsten cathodes. In 2019 Joint Meeting of the 32nd International Vacuum Nanoelectronics Conference (IVNC) and 12th International Vacuum Electron Sources Conference (IVESC) IEEE.
- Chen, D., Jacobs, R., Morgan, D., Booske, J., Lau, Y.Y. and Jassem, A., 2019. A study of the physics of Miram curves. In APS Division of Plasma Physics Meeting Abstracts (Vol. 2019, pp. TO7-006).
- Chen, D., Jacobs, R., Morgan, D. and Booske, J., 2020, October. First-principles model of Miram curve from polycrystalline tungsten cathodes. In 2020 International Conference on Vacuum Electronics (IVEC) (pp. 157-158). IEEE.
- Chen, D., Jacobs, R., Morgan, D. and Booske, J., 2021. The importance of patch fields in accurately modeling Miram curves. In 2021 International Conference on Vacuum Electronics (IVEC). IEEE.
- 7. Petillo, J., Ovtchinnikov, S., Jensen, A., Chernin, D., Nelson, E., <u>Chen, D.</u>, Jacobs, R., Morgan, D., Booske, J., Jassem, A. and Lau, Y.Y., 2021. Including the Effects of Spatially

- Varying Work Functions in Electron Gun Design. In 2021 22nd International Vacuum Electronics Conference (IVEC) (pp. 1-2). IEEE.
- 8. Chen, D., Jacobs, R., Morgan, D. and Booske, J., 2022. Impact of the patch fields and space charge on the shape of the Miram curve. In 2022 International Conference on Vacuum Electronics (IVEC). IEEE. (Student paper competition finalist)
- 9. <u>Chen, D.</u>, Jacobs, R., Morgan, D. and Booske, J., 2022. Physics-based model for nonuniform thermionic emission from spatially heterogeneous cathodes. Accepted to 2022 International Conference on Plasma Science (ICOPS). IEEE.

Contents

	Ack	nowledg	gments	i
	Publ	ications		ii
	Con	ference	presentations	ĺV
	Con	tents		vi
	List	of Figu	res	X
	List	of Table	es	V
	Abst	tract		vi
1	Intr	oductio		1
	1.1	Electro	on emission	1
	1.2	Therm	ionic cathodes	1
	1.3	Motiva	ation and overview	2
2	Prev	ious stu	udies on electron emission	4
	2.1	Classic	cal effects in uniform emission	4
		2.1.1	Richardson-Laue-Dushman equation	4
		2.1.2	Schottky barrier lowering effect	5
		2.1.3	Space charge effect and Child-Langmuir law	5
		2.1.4	Classical emission model for uniform emission	6
	2.2	Additi	onal Effects in the nonuniform emission	6
		2.2.1	Patch field effect	6
		2.2.2	3-D space charge effect	7
		2.2.3	Lateral momentum of electrons	7
	2.3	Empir	ical explanations of thermionic emission	7
		2.3.1	Longo-Vaughan equation	7
		2.3.2	Continuous work function treatment	8
		2.3.3	Practical work function distribution (PWFD)	8

	2.4	Summary of previous thermionic emission models	8
3	Mod	lel of nonuniform thermionic emission	10
	3.1	Introduction	10
	3.2	Model	11
	3.3	Relationship to previous models	15
	3.4	Results – Use checkerboard as example	17
		3.4.1 Checkerboard work function distribution	17
		3.4.2 $J-T$ and $J-V$ curves	17
	3.5	Conclusion	20
4	Emi	ssion measurements	22
	4.1	Emission test system	22
	4.2	Cathode operation	23
5	Mod	leling the emission from real cathodes	25
	5.1	Introduction	25
	5.2	Cathode sample	27
	5.3	Missaston to a standard and a	20
		Microstructure characterization	28
	5.4	Density functional theory work function values	
			28
		Density functional theory work function values	28 30
	5.5	Density functional theory work function values	28 30 32
	5.5	Density functional theory work function values	28 30 32 32
	5.5	Density functional theory work function values	28 30 32 32 35
	5.5	Density functional theory work function values Emission modeling	28 30 32 32 35 37
	5.5 5.6	Density functional theory work function values Emission modeling Results 5.6.1 Spatial distribution of work function 5.6.2 Emission current density 5.6.3 Two-dimensional emission map Sensitivity analysis and sources of error	28 30 32 32 35 37 40

72

	6.1	Introduction	12			
	6.2	Zebra crossing work function distribution	5			
	6.3	Effects of patch fields and space charge	1			
	6.4	Quantifying the shape of Miram curve knee	18			
	6.5	Space charge effect	;]			
	6.6	Patch field effect	<u>;</u> ∠			
	6.7	Shape of Miram curve knee	ie			
	6.8	Physical factors impacting normalized emission at TL-FSCL intersection temperature 5	3			
	6.9	Relationship to Longo-Vaughan equation)(
	6.10	Summary	<u>,</u>			
7	Disci	ussion on fitting work function value from $J-T$ curve 6	52			
	7.1	Methods	52			
	7.2	Physical effects and fitted values				
	7.3	Summary				
8	Conc	clusions and outlook 6	57			
	8.1	Summary and impact of this work	57			
	8.2	Suggestions for future directions	59			
		8.2.1 Quantum effects	9			
		8.2.2 Lateral momentum of electrons	59			
		8.2.3 Rough cathode surface	59			
		8.2.4 Electron beam simulation	/(
		8.2.5 Discussion on Richardson constant	!(
		8.2.6 Temperature-dependent work function value	'(
		8.2.7 Discussion on other data analysis methods	<u>'</u> (

References

List of Figures

3.1	Sketch of the potential energy $E_p(x, y, z')$ for a given (x, y) as a function of z' (black	
	curve). For a given position (x, y, z) (blue plus mark), its cathode-side barrier	
	$E_{-}(x,y,z)$ is marked as red cross, and its anode-side barrier $E_{+}(x,y,z)$ as green	
	cross. (a) and (b) are examples for the case of $E_{-}(x,y,z) \ge E_{+}(x,y,z)$, while (c)	
	and (d) for $E_{-}(x,y,z) < E_{+}(x,y,z)$	12
3.2	Model heterogenous emission surface characterized as a checkerboard of spatial	
	distributions of work function. In this work, values of $\phi_1=2\text{eV}$ and $\phi_2=2.5\text{eV}$	
	and square size $a = 5 \mu$ m are used	18
3.3	Predicted (a) $J-T$ (Miram) curves at applied voltage $V_{\rm AK}=500{\rm V}$ and (b) $J-V$	
	curves at temperature $T = 1400 \mathrm{K}$ with various combinations of space charge (SC),	
	patch field (PF), and Schottky barrier lowering (Sch) effects considered. (c) and	
	(d) focus on the TL-FSCL transition region of (a) and (b), respectively, for the case	
	of 3-D space charge with and without the effect of patch fields and Schottky barrier	
	lowering.	19
4.1	Sketch of the closely spaced diode testing vehicle used to measure the thermionic	
	emission current. The rectangle filled with pink is the cathode. The purple rect-	
	angles around the cathode represent the molybdenum ring used to shield the side	
	emission	24
5.1	Inverse polar figure (IPF) showing how a grain orientation is grouped into one	
	of the eight orientation groups using the nearest neighbor algorithm. The colors	
	indicate the work function values assigned to each orientation group, which are	
	the work function values of the W surface with most stable stoichiometric Ba-O	
	adsorption calculated by density functional theory (DFT)	29

5.2	(a) Electron backscatter diffraction (EBSD) inverse polar figure (IPF) of a com-	
	mercial S-type cathode after clean-up. The areas where it is considered that grain	
	orientations are unrecognized by EBSD are plotted in black. (b) Work function	
	map by assigning the density functional theory (DFT) work function value [5]	
	with a shift of $\Delta \phi = 0.176 \text{eV}$ to the grain orientation map (a) after grouping the	
	orientations into one of the eight orientation groups.	33
5.3	Experimental data (\times and $+$ symbols) of an S-type cathode compared with the	
	emission current density predicted with nonuniform emission model (lines) at dif-	
	ferent anode-cathode voltages. (a) $J-T$ curves for different anode-cathode volt-	
	ages V . The measured V values for the data points of red \times symbols are between	
	400 V and 404 V, $300 \text{ V} \le V \le 303 \text{ V}$ for yellow, $200 \text{ V} \le V \le 202 \text{ V}$ for purple,	
	and $100\mathrm{V} \le V \le 101\mathrm{V}$ for green. (b) $J-V$ curves at different temperatures	36
5.4	Emission current density maps predicted using nonuniform emission model for a	
	cathode with work function map as Fig. 5.2b at anode-cathode voltage $V = 400 \mathrm{V}$	
	and distance $d=1.132\mathrm{mm}$, at different temperatures: (a) TL region: tempera-	
	ture $T = 1149 \mathrm{K}$, average emission current density $J = 0.340 \mathrm{A/cm^2}$, (b) transition	
	region: $1250 \mathrm{K}, J = 1.234 \mathrm{A/cm^2},$ (c) transition region but with an average emis-	
	sion current density close to the full-space-charge-limited (FSCL) value: 1411 K,	
	$J = 1.525 \mathrm{A/cm^2}$, (d) FSCL region: 1521 K, $J = 1.552 \mathrm{A/cm^2}$	39

5.5	Boxplots showing the variability of the emission current density predicted (a)
	from the submaps of different characterized area sizes at temperature $T = 1250 \mathrm{K}$,
	anode-cathode voltage $V = 400\mathrm{V}$ and distance $d = 1.132\mathrm{mm}$, (b) from a work
	function map by applying $\phi(hkl) = \phi_{\mathrm{DFT}}(hkl) + \Delta\phi(hkl)$ to the grain orientation
	map in Fig. 5.2a, where the shift values are independent and identically distributed
	(i.i.d.) following the normal distribution $\Delta\phi(hkl)\sim N(0.176\mathrm{eV},\sigma_{\mathrm{DFT}}^2)$. In a box-
	plot, the red line in the box indicates the median value. The lower edge of the box
	is the first quartile (Q_1 or 25th percentile). The upper edge is the third quartile (Q_3
	or 75th percentile). The interquartile range (IQR) is defined as $IQR = Q_3 - Q_1$.
	Data points larger than $Q_3 + 1.5$ IQR or smaller than $Q_1 - 1.5$ IQR are considered
	as outliers and plotted individually using the $+$ symbols. The whiskers extend to
	the most extreme data points not considered to be outliers
6.1	Model heterogeneous emission surface characterized as a "zebra crossing" spatial
	distribution of work function in a laterally infinite parallel diode

6.2	Schematic figures illustrating the effects of patch fields and 3-D space charge in	
	different regions: (a) temperature-limited (TL) region, (b) transition region, (c)	
	transition region with an average emission current density close to full-space-	
	charge-limited (FSCL) value, and (d) FSCL region. The anode (not shown in the	
	figures) is far away onabove the top of each subfigure, and the cathode is on the	
	bottom of each subfigure, with a low work function patch (2eV) surrounded by	
	high work function patches (2.5 eV). Dashed black curves are the equipotential	
	curveontours of the electrostatic potential (unit: V). The red and green solid curves	
	are the electric flux lines. The red ones are for the electric flux lines starting from	
	the anode while the green ones for those starting from the cathode. The dotted vio-	
	let curves indicate the position of voltage minimum $z_{\rm m}(x,y)$ (position of the virtual	
	cathode). The plots beneath each subfigure (solid violet curves) show the value of	
	the voltage minimum in front of different location of the cathode surface $V_{\rm m}(x,y)$.	
	The value of $V_{\rm m}(x,y)$ on the left half (not plotted) is symmetric to the right half.	
	The local emission current density is $J(x,y) = AT^2 \exp[-eV_m/(k_BT)]$	49
6.3	Schematic plot illustrating the definition of the TL-FSCL intersection temperature	
	T_i (dashed blue line) and the normalized intersection emission parameter α . In this	
	plot, $\alpha = J(A)/J(B)$. The solid black curve is the Miram curve $J(T)$. The dotted	
	red curve is the full-space-charge-limited (FSCL) extrapolation $J_{\rm FSCL}$. The dotted	
	green curve is the temperature-limited (TL) extrapolation J_{TL}	50

6.4	Predicted Miram curves by limiting-case (LC) theories (dashed sky-blue curve for	
	space charge limiting case, dashed magenta curve for patch field limiting case)	
	compared with the simulation results of nonuniform emission model (solid black	
	curve), from a zebra crossing work function distribution, with $\phi_1 = 2 \text{eV}$, $d = 1 \text{mm}$,	
	$V = 500\mathrm{V}$. The dotted green and red curves are the TL and FSCL extrapolation,	
	respectively. The "o" and "x" symbols indicate the TL-FSCL intersection temper-	
	ature T_i calculated using Eq. 6.2. " \circ " is the Point A in Fig. 6.3, while " \times " is Point	
	B. Different subfigures have different values of ϕ_2 and the stripe width a , as shown	
	in the title of each subfigure.	57
6.5	The normalized intersection emission parameter α as a function of the three main	
	physical parameters. (a) Space-charge-restricted α_{SC} only depends on the nor-	
	malized work function difference $(\phi_1 - \phi_2)/(k_{\rm B}T_{\rm i})$ and the patch-diode size ratio	
	a/d . (b) Patch-field-restricted $\alpha_{\rm PF}$ only depends on the normalized work function	
	difference $(\phi_1 - \phi_2)/(k_{\rm B}T_{\rm i})$ and the patch-diode field ratio $E_{\rm patch}/E_{\rm AK} = [(\phi_1 - \phi_2)/(k_{\rm B}T_{\rm i})]$	
	$\phi_2)/(ea)]/(V_{ m AK}/d)$. The right vertical axis is the value of the corresponding Longo	
	parameter n , obtained from the relationship $\alpha = 2^{-1/n}$	59
6.6	Comparison between the results of our limiting-case (LC) theoretical models (dashed	
	sky-blue curve for theory of space charge, dashed magenta curve for patch fields)	
	and the simulation (solid black) of zebra crossing work function distributions with	
	$\phi_1 = 2_{\text{eV}}, \phi_2 = 2.5_{\text{eV}}, d = 1 \text{mm}, V = 500 \text{V}, \text{and various a values.}$ The right ver-	
	tical axis is the value of the corresponding Longo parameter n , obtained from the	
	relationship $\alpha = 2^{-1/n}$	60
7.1	Example of fitting $A_{\rm fit}/A_{\rm theory}$ and ϕ from experimental dataset. (a) is a $J-T$ plot.	
	(b) is the corresponding $\log J - 1/T$ plot. Experimental data here are the same as	
	Fig. 5.3	62

7.2 Relation between the fitted ϕ versus two key parameters associated with the parameters as of the parameters as the parameters as of the para		
	field effect. (a) is from doing linear fit on the nonuniform emission model results on	
	a zebra crossing work function distribution model with parameters ranging within	
	Eq. 7.2. (b) is the results from the limiting-case analytic study	64
7.3	Scatter plot of fitted ϕ value versus $A_{\rm fit}/A_{\rm theory}$. Data are from doing linear fit on the	
	nonuniform emission model results on a zebra crossing work function distribution	
	model with parameters ranging within Eq. 7.2	65
7.4	Example that the fitted work function value is lower than any local work function	
	values. (a) is a $J-T$ plot. (b) is the corresponding $\log J - 1/T$ plot	66

List of Tables

1.1	Types of electron emission	1
2.1	History of thermionic emission models	9
5.1	List of the eight orientations with work function values predicted using density	
	functional theory (DFT). ϕ_{DFT} is the DFT work function value for the most stable	
	stoichiometric Ba-O adsorption for each orientation. $\phi_{\mathrm{DFT}} + \Delta \phi$ is the shifted work	
	function value where the shift is $\Delta \phi = 0.176\mathrm{eV}$. The "Percentage" column shows	
	the percentage of each orientation group in Fig. 5.2	34
6.1	Values of the parameters in the cases in Fig. 6.4	56

Abstract

Emission current density is a key property to describe the behavior of thermionic emission. Experimental observations have long-established that there exists a smooth roll-off or knee transition between the temperature-limited (TL) and full-space-charge-limited (FSCL) emission regions of the emission current density-temperature J-T (Miram) curve, or the emission current density-voltage J-V curve for a thermionic emission cathode.

I developed a physics-based nonuniform thermionic emission model, incorporating 3-D space charge, patch fields, and Schottky barrier lowering effects. The model is capable to predict both the J-T and J-V curves from a given work function distribution. The results from this model illustrates that the smooth TL-FSCL transition arises as a natural consequence of the physics of nonuniform thermionic emission, and that *a priori* assumptions or empirical equations are not needed.

As a further study, I apply this nonuniform emission model on real cathodes. The predicted results are consistent with experimental observations, including the TL-FSCL transition.

The shape of Miram curves is an important figure of merit for thermionic vacuum cathodes. I developed limiting-case analytic models on the shape of Miram curves, showing that there are three main physical parameters which significantly impact the shape of the Miram curve.

As another further study using the nonuniform emission model, I evaluated the approach to simultaneously fit both the Richardson constant and the work function value from dataset in TL region, showing it can be misleading to only report the fitted work function value without paying attention to the fitted Richardson constant.

My studies on the nonuniform thermionic emission include theoretical studies, numerical simulation, and experiments. My nonuniform thermionic emission model is the first physics-based model able to predict the J-T and J-V curves comparable with experimental observations. This physics-based study connects the emission current density to the cathode surface microstructure and provides new understanding and a guideline to the analysis of experimental emission data, the manufacturing of cathodes, and the design of vacuum electronic devices.

1 Introduction

1.1 Electron emission

If the electrons move from a material to the vacuum, it is called the electron emission. There are multiple types of electron emission, depending on the source of the electron energy. (Table 1.1)

Table 1.1: Types of electron emission

Emission	Source of electron energy
Thermionic emission	Heat
Field emission	A high applied electric field
Photoemission	Photon
Secondary emission	Primary electrons

However, in the actual applications of thermionic emission, there is almost always an applied electric field. Even though such an electric field is usually too small to cause quantum tunneling effect, it is able to lower the barrier for the electrons, which is known as the Schottky effect. If the Schottky effect is significant, such emission is also called as the field enhanced thermionic emission or Schottky emission.

In my PhD work, I focus on the thermionic emission, including the Schottky effects, where quantum tunneling effect is negligible.

1.2 Thermionic cathodes

The material where the electrons emit from is called the cathode. The cathode in thermionic emission is called thermionic emission. Thermionic cathodes provide the electron source in numerous vacuum electronic devices (VEDs) used in civilian, industrial, and scientific applications, such as communication devices, ion thrusters, thermionic energy converters, and free electron lasers.[1, 2, 3]

There are many types of thermionic cathodes, among which the cathodes based on porous, polycrystalline W combined with mixtures of metal oxides (typically BaO-CaO-Al₂O₃) marked a significant evolutionary step in the history of thermionic cathodes, as these dispenser cathodes produce high-current-density emission with long lifetime due to their dynamically stable, lowwork-function surfaces.[4] There are some widely-used mixture ratios for the metal oxides in the dispenser cathodes. The most common mix is BaO: CaO: $Al_2O_3 = 5:3:2$ (a B-type cathode) which produces emission current densities of several A/cm². There are other variations including the 4:1:1 cathode (S-type), which is resistant to surface poisoning and can usually be operated at a temperature 30°C lower than other types. [5, 6, 7, 8] More recent dispenser cathodes include the M-type and scandate cathodes, which have a lower effective work function than the B- and S-type cathodes.[9, 10, 11] The B-, S- and M-type cathodes have constituted the majority of commercial thermionic cathodes for the past 50 years and are used as the electron sources in numerous vacuum electronic devices (VEDs) such as communication devices, ion thrusters, thermionic energy converters, and free electron lasers. These applications, taken together, influence multiple facets of our modern life, ranging from defense, satellite communications, radar, and scientific research, to industrial-scale food production and manufacture of heat-harvesting renewable energy technology.[1, 2]

1.3 Motivation and overview

The total emission current density divided by the cathode area, referred to as the cathode-averaged emission current density, J, is a key property in thermionic emission. J is affected by many parameters including temperature T, anode-cathode voltage V, diode geometry, etc. It is important to know the relation between J and T and V when other parameters are fixed. J-T curves for fixed V values and J-V curves for fixed T values are usually used to evaluate the J(T,V) relation. Experimental observations have long-established that there exists a smooth roll-off or knee transition between the temperature-limited (TL) and full-space-charge-limited (FSCL) emission regions of the emission current density-temperature J-T (Miram) curve, or the emission current

density-voltage J-V curve for a thermionic emission cathode. However, before my study, there was no physics-based model able to predict the J(T,V) relation comparable with the experimental observations.

Experimental results including thermionic electron emission microscopy (ThEEM) images reveal that polycrystalline cathodes have a spatial distribution of work function and emit nonuniformly. [12, 13, 14, 15] Building a physics-based emission model unifying all important physical effects is important in the nonuniform emission from heterogeneous cathode surface, as it is helpful for studying nonuniform thermionic emission as it enables the in-depth understanding of the impact of nonuniform thermionic emission on the TL-FSCL transition. This type of modeling can increase understanding of the interplay of different contributions to emission physics, the materials engineering of cathodes including not only bulk polycrystalline cathodes but also novel cathodes like those based on 2D materials (e.g. graphene)[16, 17], and the design of devices employing electron emission cathodes.

2 Previous studies on electron emission

2.1 Classical effects in uniform emission

The theory of thermionic emission has been studied for more than a century. The simplest physical model for a thermionic cathode is a perfectly smooth cathode surface with a single work function value ϕ , referred to as a "uniform cathode" in this paper. The physics of the thermionic emission from an infinitely large uniform cathode in a parallel diode has been thoroughly studied. In this subsection, I will discuss the non-quantum, non-relativistic effects in uniform electron emission, referred to as "classical" here.

However, such predicted TL-FSCL transition from a uniform cathode is sharp, qualitatively different from the experimental results of actual thermionic cathode emission measurements,[18] which are characterized by a smooth, more gradual TL-FSCL transition in the Miram and the I-V curves.

2.1.1 Richardson-Laue-Dushman equation

The Richardson-Laue-Dushman equation[19, 20] is widely used to describe the temperature-limited (TL) emission current density of a uniform thermionic cathode at no applied electric field:

$$J_{\rm RLD} = AT^2 \exp\left(-\frac{\phi}{k_{\rm B}T}\right) \tag{2.1}$$

where ϕ is the work function, T is the temperature, $k_{\rm B}$ is the Boltzmann constant. The Richardson constant is $A = 4\pi mek_{\rm B}^2/h^3$ where h is the Planck constant.

Although electrons actually follow Fermi-Dirac distribution, for thermionic emission, we have $\phi \gg k_{\rm B}T$. Therefore, the discrepancy in the final results between the Maxwell-Boltzmann distribution assumption and the Fermi-Dirac distribution is negligible. While in some books[21], the authors introduce the Richardson-Laue-Dushman equation using Fermi-Dirac distribution and some mathematical approximation, such calculation is equivalent to using Maxwell-Boltzmann

distribution with some assumptions and concepts from the old quantum theory.

2.1.2 Schottky barrier lowering effect

The potential energy is not a sharp transition at the metal-vacuum interface. Due to many factors including the electron interaction, the potential energy E_p as a function of the distance to the interface z is smooth. While such a smooth function $E_p(z)$ can be estimated with quantum mechanics[22], the image charge potential[23] is a good classical approximation.

Considering the Schottky barrier lowering effect near the cathode surface, the potential energy E_p takes the form:

$$E_{\rm p}(x, y, z) = -eV(x, y, z) - \frac{e^2}{16\pi\varepsilon_0 z}$$
 (2.2)

where V(x,y,z) is the electrostatic potential. The additional energy term $-\frac{e^2}{16\pi\varepsilon_0 z}$ is the image charge potential term, representing the Schottky effect.

The Richardson-Laue-Dushman equation with Schottky barrier lowering correction describes the temperature-limited (TL) emission current density of a uniform cathode.

2.1.3 Space charge effect and Child-Langmuir law

The Child-Langmuir law[24, 25] provides a model of the full-space-charge-limited (FSCL) emission under the assumption that all electrons have zero initial velocity:

$$J_{\rm CL} = \frac{4\varepsilon_0}{9} \sqrt{\frac{2e}{m}} \frac{V^{3/2}}{d^2}$$
 (2.3)

where ε_0 is the vacuum permittivity, e is the elementary charge, m is the electron mass, V is the anode-cathode voltage, and d is the anode-cathode distance.

Later, Langmuir and Fry's studies[25, 26] provide a model under the assumption that the initial velocities of the electrons follow Maxwell-Boltzmann equation. In particular, in the transition case

that the net electric field at the cathode surface is zero, the emission current density is

$$J_{\text{CLT}} = \frac{4\varepsilon_0}{9} \sqrt{\frac{2e}{m}} \frac{V^{3/2}}{d^2} \frac{9}{8\sqrt{\pi}} \eta^{-3/2} \left(\int_0^{\eta} \frac{d\eta}{\sqrt{\text{erfcx}}\sqrt{\eta} - 1 + 2\sqrt{\eta/\pi}} \right)^2$$
 (2.4)

where $\eta = eV_{\rm AK}/(k_{\rm B}T)$, and erfcx is the scaled complementary error function.

2.1.4 Classical emission model for uniform emission

Richardson-Laue-Dushman equation, Schottky barrier lowering effect, and Langmuir and Fry's studies form the classical theory of uniform thermionic emission. Scott's and Eng's [27, 18] unified these three theories, which is able to predict the J(T,V) relation, not only the TL and FSCL regions but also the TL-FSCL transition region. In their work, they also pointed out that there is still some discrepancy between their model with experimental observations, which indicate that more physical effects need to be considered to predict the J(T,V) relation for actual cathodes.

2.2 Additional Effects in the nonuniform emission

2.2.1 Patch field effect

The work function ϕ is defined as the difference between the Fermi level $E_{\rm F}$ and the vacuum level $E_{\rm vacuum}$. For a conductive cathode, at thermodynamic equilibrium, the cathode shares the same Fermi level. In the case that the cathode has a spatially heterogeneous work function distribution, for example, $\phi(x,y)$, then the cathode surface will have a spatially nonuniform vacuum level distribution: $E_{\rm vacuum}(x,y) = E_{\rm F} + \phi(x,y)$, which causes an additional electric field between different work function patches. Such an effect is called the patch field effect. [18, 28, 29, 30]

2.2.2 3-D space charge effect

The electrons traveling between the cathode and the anode can also cause electric fields. Such effect is called 3-D space charge effect, and can be describe with 3-D Poisson's equation:

$$\nabla^2 V(x, y, z) = -\frac{\rho(x, y, z)}{\varepsilon_0}$$
 (2.5)

where V is the electrostatic potential, ρ is the charge density, and ε_0 is the vacuum permittivity. The 3-D space charge effect has been well studied and discussed in [31, 32].

2.2.3 Lateral momentum of electrons

Lateral momentum of electrons is another effect in nonuniform emission. However, a key result from the work of Chernin et al.[31] is that the lateral motion of electrons has only a minor effect on predictions of averaged emission current density from an infinitely large cathode in an infinite parallel diode when the 3-D space charge effect is considered. Therefore, it is still possible to accurately predict the averaged emission current density under the assumption that the electrons are restricted to move one-dimensionally from the cathode to the anode with no lateral momentum, which is equivalent to assuming an infinite magnetic field is present along the anode-cathode direction.

2.3 Empirical explanations of thermionic emission

2.3.1 Longo-Vaughan equation

Longo-Vaughan equation[33, 34] is a well-known empirical equation which is able to smoothly connect the TL and FSCL region:

$$J^{-n} = J_{\text{TL}}^{-n} + J_{\text{FSCL}}^{-n} \tag{2.6}$$

where n is the Longo parameter.

Vaughan pointed out that well-designed and well-made guns have n values in the range 6 to 10,

while the diodes with patchy emission, uneven heating or other defects have 2 < n < 5 range.[34]

2.3.2 Continuous work function treatment

Another empirical method to obtain a smooth TL-FSCL transition is to *a priori* assume that the cathode surface has a continuous distribution of work function values.[21] Such work function distribution can lead to a smooth TL-FSCL transition even under the assumption that different patches on the cathode surface do not interact with each other.

2.3.3 Practical work function distribution (PWFD)

The practical work function distribution (PWFD) method[35] is a mathematical treatment to convert a J-T curve to a curve looking like a work function distribution. PWFD was obtained in this way:

1. For a J(T) curve, use Richardson-Laue-Dushman equation (Eq. 2.1) to solve the work function value $\phi(T)$.

2. Define
$$f(T) = \begin{cases} \frac{J}{J_{\text{FSCL}}}, & \frac{J}{J_{\text{FSCL}}} \leq \frac{1}{2} \\ 1 - \frac{J}{J_{\text{ESCL}}}, & \frac{J}{J_{\text{ESCL}}} > \frac{1}{2} \end{cases}$$

3. The $f(\phi)$ plot is the PWFD curve.

PWFD curves are often used to evaluate the cathode lifetime[35] and were not intended to indicate the actual work function distribution.

2.4 Summary of previous thermionic emission models

Table 2.1 summarize the list of the previous physics-based thermionic emission models compared with my work. Although there are some empirical explanations of the smooth TL-FSCL

transition before my study, there is no physics-based model able to predict the TL-FSCL transition as smooth as the experimental observations.

I will show the results of my model in the following chapters.

Table 2.1: History of thermionic emission models

	Space	Patch field	Schottky effect	References
II.:'C	no	no	no	Richardson-Laue-Dushman (RLD) equation[36, 20]
Uniform	no	no	with	RLD equation with Schottky effect[23]
cathode studies	1-D	no	no	Child-Langmuir law[24, 25] with finite temperature correction[26, 25]
	1-D	no	with	Scott and Eng's work[27, 18]
	no	with	no	RLD equation with patch field effect[12, 13]
None iform	no	with	with	Anomalous Schottky effect[30]
Nonuniform	3-D	no	no	1.5-D model[31] and 2.5-D model[32]
cathode	3-D	no	with	
studies	3-D	with	no	My work[37]
	3-D	with	with	

3 Model of nonuniform thermionic emission

This chapter comes from [37], first-authored by me. I am the lead researcher of this topic.

3.1 Introduction

It is known that the nonuniform thermionic emission in a parallel diode is subject to the effects of 3-D space charge[31, 32, 16], patch fields[12, 13], Schottky barrier lowering[23], and the lateral motion of electrons[31, 38, 39]. By patch field effect, I refer to a nonuniform electrostatic potential on the cathode surface based on local work function values. [12, 13, 40, 28, 29] This local, nonuniform, electrostatic potential distribution results from the microscopic, lateral transfer of conduction electrons between grains having different work functions, in order to equalize the Fermi energy between all contacting, conducting grains. Each of these effects has been studied in detail separately. While there is still no general, physics-based model unifying all of these effects, previous efforts have made advances in combining some subsets of the effects together. For example, the theory of the anomalous Schottky effect unifies the effects of patch fields and Schottky barrier lowering, [30] and recent studies [31, 39] discuss the effects of 3-D space charge and the lateral motion of electrons. A key result from the work of Chernin et al.[31] is that the lateral motion of electrons has only a minor effect on predictions of averaged emission current density from an infinitely large cathode in an infinite parallel diode when the 3-D space charge effect is considered. Therefore, it is possible to accurately predict the averaged emission current density under the assumption that the electrons are restricted to move one-dimensionally from the cathode to the anode with no lateral momentum, which is equivalent to assuming an infinite magnetic field is present along the anode-cathode direction.

I develop a physics-based nonuniform thermionic emission model unifying the effects of 3-D space charge, patch field effects, and Schottky barrier lowering. Based on the work from Chernin et al.[31], I neglect the lateral motion of electrons. I note here that the lateral motion of electrons may have a larger effect in some extreme cases, for example where the emitting patches of the

cathode have a length scale comparable to the anode-cathode distance, but we do not consider that case here. My nonuniform emission model is able to predict the entire domain of the J-T (Miram) and the J-V curves including the TL-FSCL transition for a heterogeneous cathode surface in a perfect infinite parallel diode. Our model results demonstrate that the smooth and gradual TL-FSCL transitions observed in experiments can be reproduced by the model and are natural consequences of the physics of nonuniform thermionic emission. We are therefore able to reproduce the experimentally observed smooth and gradual TL-FSCL transition without relying on any empirical equations such as the Longo-Vaughan equation[33, 34] or an a priori assumption of a continuous distribution of work functions[41] on the cathode surface.

3.2 Model

For the model of thermionic emission from heterogeneous surfaces developed in this work, the cathode is located at z = 0, and the anode at z = d, where d is the anode-cathode distance. It is assumed that the distribution of the electron energies follows a Maxwell-Boltzmann distribution, and that the motion of the electrons between the cathode and the anode follows non-relativistic classical electrodynamic behavior. The total energy for each electron is conserved: $E = E_p(x,y,z) + mv^2/2$, where $E_p(x,y,z)$ is the potential energy at position (x,y,z), m is the mass of an electron, and v is the velocity. In the absence of an energy barrier at the surface of the cathode, the emission current density at position (x,y) due to electrons of energy between E and E + dE has the form:[18]

$$dJ(x, y; E) = \frac{AT}{k_{\rm B}} \exp\left[-\frac{E - E_{\rm F}(x, y)}{k_{\rm B}T}\right] dE$$
 (3.1)

where $A = 4\pi mek^2/h^3$ is the Richardson constant, e is elementary charge, k_B is Boltzmann's constant, h is Planck's constant, T is temperature, and $E_F(x,y)$ is the local Fermi energy level of the cathode.

The model for the steady state electron density depends on the shape of the potential energy that is created under steady state emission. Figure 3.1 shows sketches of the potential energy

 $E_{\rm p}(x,y,z')$ for a given (x,y) as a function of z' for different cases. For a given position (x,y,z), we define the cathode-side barrier as $E_{-}(x,y,z)=\max_{0\leq z'\leq z}E_{\rm p}(x,y,z')$ and the anode-side barrier as $E_{+}(x,y,z)=\max_{z\leq z'\leq d}E_{\rm p}(x,y,z')$. The values of E_{-} and E_{+} determine how many electrons are able to reach the position (x,y,z), in the case that the lateral motion of electrons and quantum effects are neglected.

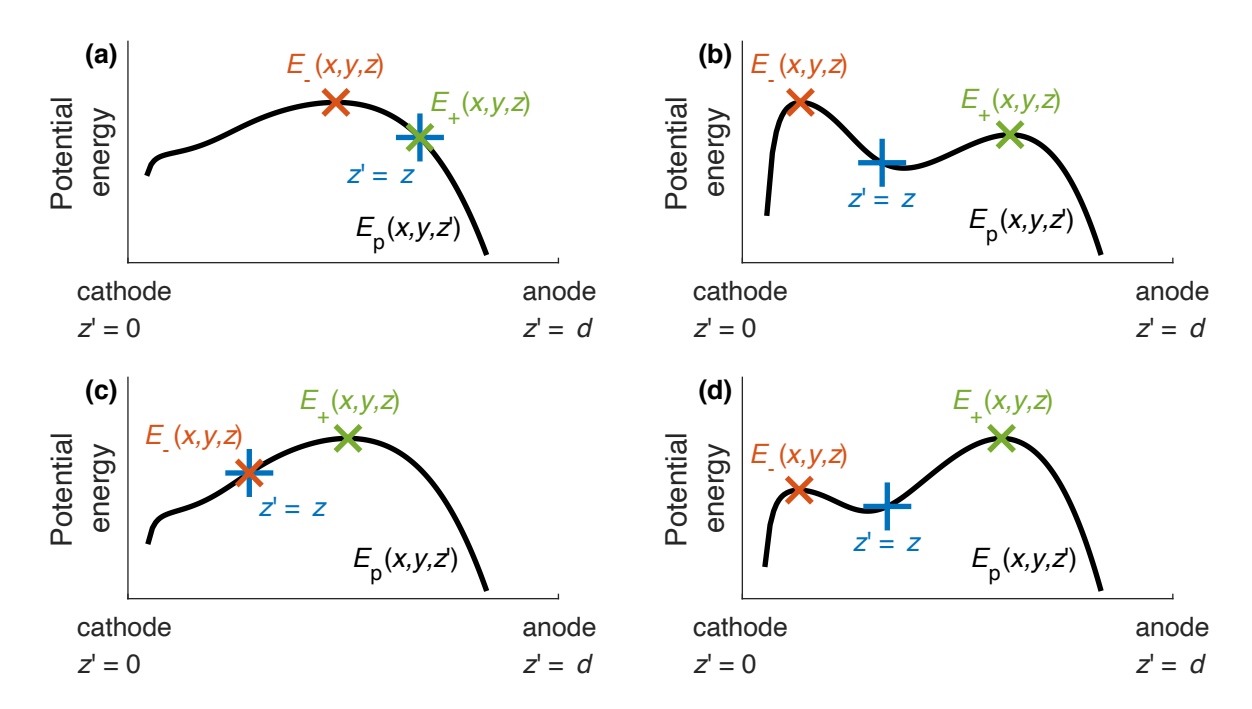


Figure 3.1: Sketch of the potential energy $E_p(x,y,z')$ for a given (x,y) as a function of z' (black curve). For a given position (x,y,z) (blue plus mark), its cathode-side barrier $E_-(x,y,z)$ is marked as red cross, and its anode-side barrier $E_+(x,y,z)$ as green cross. (a) and (b) are examples for the case of $E_-(x,y,z) \ge E_+(x,y,z)$, while (c) and (d) for $E_-(x,y,z) < E_+(x,y,z)$.

Considering the positions (x, y, z) satisfying $E_{-}(x, y, z) \ge E_{+}(x, y, z)$, electrons emitted from the cathode surface at position (x, y, 0) with energy $E \ge E_{-}$ can pass through the cathode-side barrier and reach the position (x, y, z) as they move toward the anode. The charge density for positions (x, y, z) where $E_{-}(x, y, z) \ge E_{+}(x, y, z)$ has the form:

$$\rho(x, y, z) = -\int_{E=E_{-}}^{\infty} \frac{\mathrm{d}J}{v} = -\int_{E=E_{-}}^{\infty} \frac{\mathrm{d}J}{\sqrt{2(E - E_{\mathrm{p}})/m}}, \quad E_{-}(x, y, z) \ge E_{+}(x, y, z)$$
(3.2)

where the electron velocity $v = \sqrt{2(E - E_p)/m}$.

However, for any position (x,y,z) where $E_-(x,y,z) < E_+(x,y,z)$, electrons emitted from the cathode surface at (x,y,0) with energy $E \ge E_-$ can still pass through the cathode-side barrier and reach the position (x,y,z). Electrons with energy $E_- \le E < E_+$ will be reflected back toward the cathode by the higher anode-side barrier and pass through the location (x,y,z), this time moving back toward the cathode. Therefore, the charge density for positions (x,y,z) where $E_-(x,y,z) < E_+(x,y,z)$ has the form:

$$\rho(x,y,z) = -\left[\int_{E=E_{-}}^{\infty} \frac{\mathrm{d}J}{\sqrt{2(E-E_{\mathrm{p}})/m}} + \int_{E=E_{-}}^{E_{+}} \frac{\mathrm{d}J}{\sqrt{2(E-E_{\mathrm{p}})/m}}\right], \quad E_{-}(x,y,z) < E_{+}(x,y,z)$$
(3.3)

Substituting Equation 3.1 into Equations 3.2 and 3.3, we obtain a closed-form expression of the relation between the potential energy $E_p(x, y, z)$ and the charge density $\rho(x, y, z)$:

$$\rho(x,y,z) = \begin{cases} -\sqrt{\frac{\pi m}{2k_{\rm B}T}} A T^2 \exp\left(-\frac{E_{\rm p} - E_{\rm F}}{k_{\rm B}T}\right) \operatorname{erfc} \sqrt{\frac{E_{-} - E_{\rm p}}{k_{\rm B}T}}, & E_{-}(x,y,z) \ge E_{+}(x,y,z) \\ -\sqrt{\frac{\pi m}{2k_{\rm B}T}} A T^2 \exp\left(-\frac{E_{\rm p} - E_{\rm F}}{k_{\rm B}T}\right) \left[2 \operatorname{erfc} \sqrt{\frac{E_{-} - E_{\rm p}}{k_{\rm B}T}} - \operatorname{erfc} \sqrt{\frac{E_{+} - E_{\rm p}}{k_{\rm B}T}}\right], \\ E_{-}(x,y,z) < E_{+}(x,y,z) \end{cases}$$
(3.4)

where erfc is the complementary error function. The electrostatic potential V and the charge density ρ satisfy Poisson's equation, and therefore the 3-D space charge effect is included in this model through:

$$\nabla^2 V(x, y, z) = -\frac{\rho(x, y, z)}{\varepsilon_0}$$
(3.5)

where ε_0 is the vacuum permittivity.

The boundary condition for the cathode surface is:[18, 28, 29, 30]

$$V(x, y, z = 0) = -\frac{E_{F}(x, y) + \phi(x, y)}{e}$$
(3.6)

where $E_{\rm F}(x,y)$ and $\phi(x,y)$ are the local Fermi level and the local work function of the cathode,

respectively.

Similarly, the boundary condition for the anode surface is:[18]

$$V(x, y, z = d) = -\frac{E_{F,anode}(x, y) + \phi_{anode}(x, y)}{e}$$
(3.7)

where $E_{F,anode}(x,y)$ and $\phi_{anode}(x,y)$ are the local Fermi level and the local work function of the anode, respectively.

At thermodynamic equilibrium, the Fermi level is equal throughout a conductor. In the case of a conductive cathode and a conductive anode, $E_{\rm F}(x,y)$ is a constant value throughout the cathode and $E_{\rm F,anode}(x,y)$ is a constant value throughout the anode. Neglecting the thermoelectric effect, which is no larger than tens of millivolts under typical operating conditions and negligible compared to the typical applied anode-cathode voltage, the anode-cathode Fermi level difference is $E_{\rm F,anode}-E_{\rm F}=-eV_{\rm AK}$, where $V_{\rm AK}$ is the anode-cathode voltage as measured by a voltmeter in experiments. For the present model, if we let $E_{\rm F}=0$ then $E_{\rm F,anode}=-eV_{\rm AK}$. In this case, the boundary conditions are $V(x,y,z=0)=-\phi(x,y)/e$ and $V(x,y,z=d)=V_{\rm AK}-\phi_{\rm anode}(x,y)/e$. The cathode surface is a non-equipotential surface, and the patch field effect is included.

Considering the Schottky effect near the cathode surface, the potential energy E_p takes the form:

$$E_{\rm p}(x,y,z) = -eV(x,y,z) - \frac{e^2}{16\pi\varepsilon_0 z}$$
 (3.8)

where $-\frac{e^2}{16\pi\varepsilon_{0Z}}$ is the energy term representing the image charge effect.

The nonuniform thermionic emission model can be solved by solving the system of Equations 3.4, 3.5, 3.6, 3.7, and 3.8. A numerical method to solve this system of nonlinear equations is to solve them by iterations of $E_p \to \rho \to V \to E_p$ until convergence is obtained. One of the algorithms to solve Poisson's equation in the step $\rho \to V$ involves a Fourier transformation for the x and y directions and the Thomas algorithm for the z direction.[31, 32] Once $E_p(x,y,z)$ is solved, one is able to calculate the maximum barrier $E_{p,\max}(x,y) = \max_{0 \le z \le d} E_p(x,y,z)$, and the corresponding local

emission current density is

$$J(x,y) = AT^{2} \exp \left[-\frac{E_{p,\max}(x,y) - E_{F}(x,y)}{k_{B}T} \right]$$
 (3.9)

The averaged emission current density of the cathode can be obtained by averaging J(x,y) over the whole cathode surface.

3.3 Relationship to previous models

In the following results, we analyze the predicted emission from our model and evaluate how each physical effect impacts the emission by comparing the results for the cases where some subset or all of the three physical effects are considered. We note here that all three effects of 3-D space charge, patch fields, and Schottky barrier lowering are physically present in nonuniform thermionic emission. Although neglecting any of them will make the emission model less physical, we show the results where some of the effects are neglected to illustrate the impact of each effect on the resulting emission.

The patch field effect was neglected in previous studies which included the 3-D space charge effect.[31, 32, 39] To evaluate the importance of the patch field effect, we show the results under a no-patch-field situation equivalent to the methods used in those previous studies[31, 32, 39]. The patch field effect originates from the fact that patches with different work functions will have different local (near-surface) vacuum level energies (different electrostatic potentials on the cathode surface). When placed in electrically conducting contact, there will be transfer of conduction electrons between the grains so that all Fermi energies are made equal. This electron transfer results in local nonuniform electrostatic potential values in the vacuum, immediately above the grains having initially different work functions. This effect is very much related to the contact potential difference that arises at an interface between metals with dissimilar work functions. Grains starting with an initially higher work function (lower Fermi energy) will acquire slightly greater local electron charge and acquire a local electrostatic potential depression relative to their lower work function

neighboring grains, which results in the electrostatic potential nonuniformity on the cathode surface based on local work function values. To correctly predict the spatially nonuniform emission energy barrier, one needs to apply a nonuniform electrostatic potential distribution to the surface, where the local "cathode" potential is more or less negative in proportion to the local work function of each grain, relative to the common Fermi level (nominal cathode voltage) of the cathode (Equation 3.6). Thus, if the nominal cathode voltage is assumed to be at a reference zero volts, then the surface (vacuum) electrostatic potential value of a $2.0 \,\mathrm{eV}$ work function grain assumes a $-2.0 \,\mathrm{V}$ potential value whereas a $2.5\,\mathrm{eV}$ work function grain assumes a $-2.5\,\mathrm{V}$ potential value. The nopatch-field results are obtained under the assumption that the cathode surface have the same local near-surface vacuum level, i.e., the boundary condition V(x, y, z = 0) is constant throughout the cathode surface, so there will be no patch field effect. In no-patch-field cases, we assume that the boundary condition of the cathode surface is $V(x,y,z=0)=-\bar{\phi}/e$, where $\bar{\phi}$ is the average value of $\phi(x,y)$ over the whole cathode surface, and that $E_{\rm F}(x,y) = \bar{\phi} - \phi(x,y)$. Under this assumption, the spatial distribution of work function $-eV(x,y,z=0) - E_F(x,y) = \phi(x,y)$ is still the same as the with-patch-field cases. The comparison between no-patch-field (common local vacuum-level) and with-patch-field (common Fermi-level) results will illustrate the impact of the patch field effect.

The results without the Schottky effect are obtained by omitting the image charge term $-\frac{e^2}{16\pi\varepsilon_0 x}$ in Equation 3.8.

The results without space charge are obtained by solving the maximum barrier $E_{\rm p,max}(x,y)$ at absolute zero temperature when there is no space charge, with the assumption that the maximum barrier $E_{\rm p,max}(x,y)$ remains the same at finite temperatures. The 1-D space charge effect cases illustrate the results under the assumption that the space charge forces from different work function patches do not interact with each other. The results considering the 1-D space charge effect without the patch field effect are obtained under the assumption that each patch emits independently, where we replace the 3-D Laplace operator ∇^2 in Equation 3.5 with the corresponding 1-D operator $\frac{\partial^2}{\partial z^2}$. The results considering the 1-D space charge effect with the patch field effect are obtained in the following order: (1) Solve the model with patch fields included at absolute zero temperature

to get the potential energy E_{p1} . (2) Solve the model without patch field effects at absolute zero temperature to get the potential E_{p2} . (3) Assume the additional potential energy due to patch field is $E_{PF} = E_{p1} - E_{p2}$. (4) Solve the model after replacing the 3-D Laplace operator ∇^2 in Equation 5 with the corresponding 1-D operator $\frac{\partial^2}{\partial z^2}$ and adding a term E_{PF} to the right side of Equation 3.8.

3.4 Results – Use checkerboard as example

3.4.1 Checkerboard work function distribution

In this work, we use an idealized model heterogeneous surface characterized by an infinitely large, periodic checkerboard spatial distribution of work functions, as shown in Figure 3.2. Similar checkerboard distributions have been used in many previous studies of nonuniform emission.[12, 13, 32, 39, 42, 43] Here, a checkerboard model surface with work function values of $\phi_1 = 2 \,\mathrm{eV}$ and $\phi_2 = 2.5 \,\mathrm{eV}$ and with square size $a = 5 \,\mu\mathrm{m}$ is used. These work function values are typical values for sintered porous tungsten (dispenser) cathodes and the square size is the typical grain size.[3, 38, 8, 4] The anode-cathode distance d is chosen to be 1 mm, typical in closely spaced diode tests[44], which is much larger than patch size a. The work function of the anode is chosen to be $\phi_{\mathrm{anode}}(x,y) = 4.5 \,\mathrm{eV}$, which is close to the work function value of many anode materials including stainless steel, Monel, copper, tungsten, and molybdenum.[45]

3.4.2 J-T and J-V curves

Figure 3 contains predicted J-T (Miram) and J-V (or I-V) curves separately showing the effect of space charge at the level of 1-D and 3-D, patch fields, and Schottky barrier lowering on the resulting emission current density. From Figure 3, some qualitative, general features of the current density as a function of T and V emerge based on the inclusion of different physical effects. The inclusion of space charge effects reduces the total emission, where 1-D space charge results in greater reduction in total emission than 3-D space charge. The inclusion of patch fields also reduces the total emission. Finally, the Schottky effect increases the emission by reducing

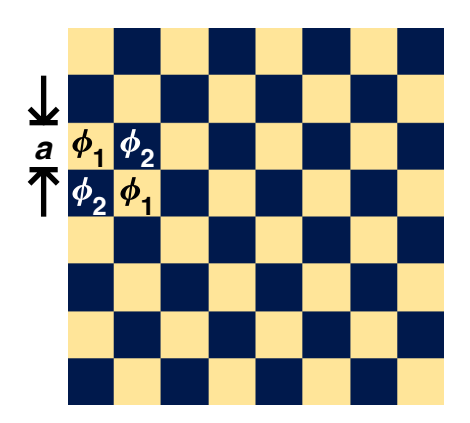


Figure 3.2: Model heterogenous emission surface characterized as a checkerboard of spatial distributions of work function. In this work, values of $\phi_1 = 2 \,\text{eV}$ and $\phi_2 = 2.5 \,\text{eV}$ and square size $a = 5 \,\mu\text{m}$ are used.

the emission surface barrier. These general findings are consistent with a number of previous studies[23, 25, 26, 27, 18, 31].

In the predicted J-T curves (Figure 3a), all of the J-T curves with no space charge effects (dotted curves) increase exponentially. This behavior occurs regardless if the patch field and Schottky effects are considered, and approximately follows the behavior of the Richardson-Laue-Dushman equation. Results of 1-D space charge without the patch field effect (dashed red and dashed blue curves) give peculiarly stepped curves qualitatively inconsistent with experiment, calling into question the assumption that each patch emits independently. Figures 3a and 3c illustrate that the 3-D space charge effect itself (solid blue curve) does not make the TL-FSCL transition region smooth in the condition similar to typical closely spaced diode tests of dispenser tungsten cathodes. However, smooth TL-FSCL transition regions are observed when both 3-D space charge and patch field effects are included together (solid green and solid yellow curves). Compared with space charge and patch field effects, the Schottky effect is minor in determining the shape of the J-T curves, and only acts to make the transition slightly smoother (solid red vs. solid blue curves, and solid green vs. solid yellow curves, best observed in Figure 3c).

Figure 3b and Figure 3d show the predicted J-V curves. In Figure 3b and Figure 3d, all curves without the Schottky effect (yellow and blue curves) converge to values one would obtain from the

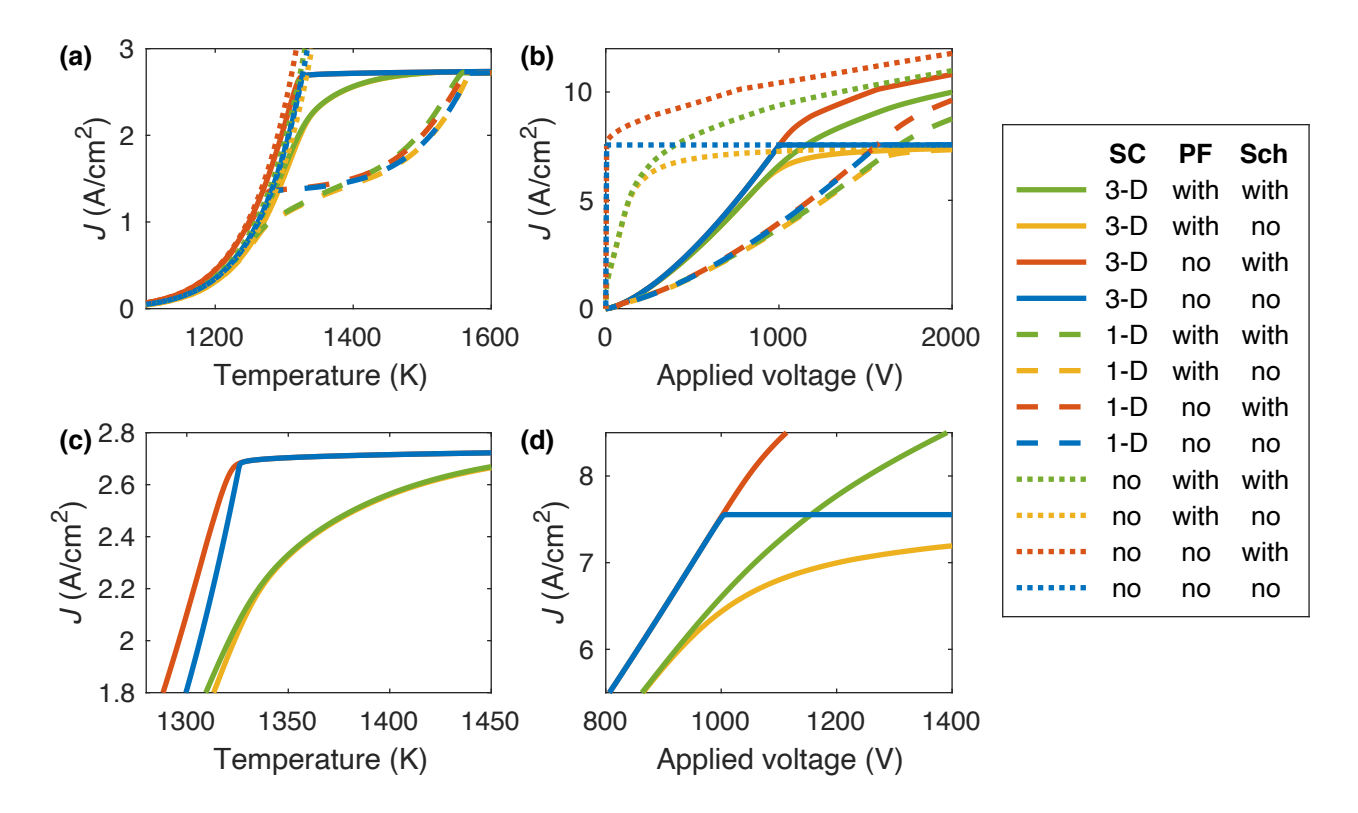


Figure 3.3: Predicted (a) J - T (Miram) curves at applied voltage $V_{\rm AK} = 500\,\rm V$ and (b) J - V curves at temperature $T = 1400\,\rm K$ with various combinations of space charge (SC), patch field (PF), and Schottky barrier lowering (Sch) effects considered. (c) and (d) focus on the TL-FSCL transition region of (a) and (b), respectively, for the case of 3-D space charge with and without the effect of patch fields and Schottky barrier lowering.

Richardson-Laue-Dushman equation at the TL regions (high voltage end). In addition, all curves with the Schottky effect included (green and red curves) show the asymptotic Schottky behavior of the current density at high voltages, as observed in experiments. The curves which ignore space charge effects (dotted curves) give the expected asymptotic behavior at the high voltage limit. Contrary to what was observed for the J-T curves, the green, yellow, and red J-V curves in Figure 3b and Figure 3d show that both patch field and Schottky effects contribute to the smoothness of the TL-FSCL transition. Although the behavior of the J-T curves with 1-D space charge (dashed curves) in Figure 3a differs substantially from typical experimental curves, the behavior of the J-V curves with 1-D space charge effects (dashed curves) in Figure 3b is qualitatively similar with the corresponding J-V curves when 3-D space charge effects are included (solid curves).

Both the J-T and J-V curves are commonly used to evaluate the cathode performance and it is therefore critical for an emission model to accurately predict the behavior of both curves. Among the twelve cases plotted in Figure 3, only the case where all the effects of 3-D space charge, patch fields, and Schottky barrier lowering are considered (solid green curves) predicts a smooth J-T (i.e., a smooth TL-FSCL transition with temperature and a smooth Miram curve knee) and J-V curve with the Schottky behavior, thereby reproducing the known experimental cathode emission behavior as both a function of temperature and applied voltage.

3.5 Conclusion

Overall, we have shown that for predicting J-T curves (also known as Miram curves), the space charge and the patch field effects (electrostatic potential nonuniformity on the cathode surface based on local work function values) play a more important role than the Schottky effect in determining the shape of the TL-FSCL transition. On the other hand, for predicting J-V curves, the patch field effect and Schottky effect are both essential to predict asymptotic Schottky behavior of the current density at high voltages.

Even with the simple heterogenous work function distribution considered in this work, consisting of only two discrete work function values, the predicted TL-FSCL transition regions are

smooth for both the J-T and J-V curves, in agreement with experimental observations on real cathodes. The present model results illustrate that a smooth TL-FSCL transition is a natural consequence of the effects of 3-D space charge, patch fields, and Schottky barrier lowering on nonuniform thermionic emission, and that neither empirical equations such as the Longo-Vaughan equation[33, 34] nor an a priori assumption of a continuous distribution of work functions on the emitting surface[41] are necessary to generate a smooth transition. This result suggests that a surface with a set of discrete work functions, perhaps associated with different surface orientation, terminations, and compositions[8, 9], could yield that smooth TL-FSCL behavior seen in actual cathodes.

Codes for the nonuniform emission model are available on GitHub (https://github.com/chendongzheng/nonuniform-emission).

4 Emission measurements

This chapter comes from [46], first-authored by me. I am the lead researcher of this topic.

4.1 Emission test system

The experimental results of emission current were measured in a closely spaced diode testing vehicle (Fig. 4.1). The heater and the anode fixtures were manufactured by L3-Harris. The anodecathode distance in this setup for a 0.97 mm high cathode was designed to be d=1.06 mm. A molybdenum ring was placed around the cathode to shield the emission from the sides. The height of the molybdenum ring was 1.14 mm, which was 0.17 mm higher than the cathode. The inner diameter (ID) 2.90 mm was 0.13 mm larger than the diameter of the cathode. The heater filament was powered by a Keithley 2200-20-5 programmable power supply which was usually operated under constant current mode.

To make it possible to measure the temperature of the cathode surfaces using a pyrometer during operation, a triode design was used with a hollow cylinder as the current collector, or "catcher". The temperature of the cathode surface was measured with a Catalogue Number 8622 optical pyrometer made by Leeds & Northrup Co., which is a $\lambda = 0.65 \,\mu$ m single-wavelength disappearing filament pyrometer. The electron emission cathode industry often simply uses the pyrometer reading to indicate the cathode temperature, reporting it as the brightness temperature. However, the true temperature of the cathode surface is needed to use our nonuniform emission model[37]. We calibrated the temperature values using Planck's law. The radiation of the cathode received by the disappearing pyrometer at wavelength λ is:

$$tr\varepsilon \frac{2hc^2}{\lambda^5} \frac{1}{e^{hc/(\lambda k_B T)} - 1} = \frac{2hc^2}{\lambda^5} \frac{1}{e^{hc/(\lambda k_B T_b)} - 1}$$
(4.1)

where T_b is the pyrometer reading (brightness temperature), T is the calibrated "true" temperature of the cathode surface to be used in the emission model, k is the Boltzmann constant, h is the Planck constant, c is the speed of light. The values of the transmissivity of the viewport t = 0.93 and the

reflectivity of the mirror r = 0.76 in the optical path were as measured. In this study, we used the emissivity value of $\varepsilon = 0.52$ recommended for impregnated W cathodes.[5] The uncertainty of the measured temperature values was approximately $\pm 20^{\circ}$ C.

During the emission measurements, the grid was biased with a PVX-4110 high voltage pulse generator made by Directed Energy (DEI), which was powered by a DC high voltage power supply made by Glassman High Voltage, Inc. with Model No. PS/ER02R150-115, and controlled by a low voltage pulse generator Model 575 pulse/delay generator made by Berkeley Nucleonics Corp (BNC). The catcher was biased with a DC high voltage power supply made by Glassman High Voltage, Inc. with Model No. PS/EQ005R240-22 and was kept more positively biased than the grid. The voltages of the grid and the catcher were measured with a LeCroy 44Xs oscilloscope. The emission current was measured with the same oscilloscope via a Model 4100C current monitor made by Pearson Electronics, Inc.

4.2 Cathode operation

The cathode was activated before the emission tests, following the instructions recommended by the cathode manufacturer, 3M Technical Ceramics. The activation process includes four steps:

- 1. Slowly increase the cathode temperature to a brightness temperature of 1000°C, and then hold this temperature for 30 minutes.
- 2. Continue to increase the cathode temperature to a brightness temperature 1175–1200 °C and hold for 1 hour.
- 3. Cool the cathode to a brightness temperature 1100–1150 °C and hold for 2 hours.
- 4. Reduce cathode temperature and measure the emission current while cooling down the cathode. The pressure was kept below 5×10^{-6} torr during the activation process.

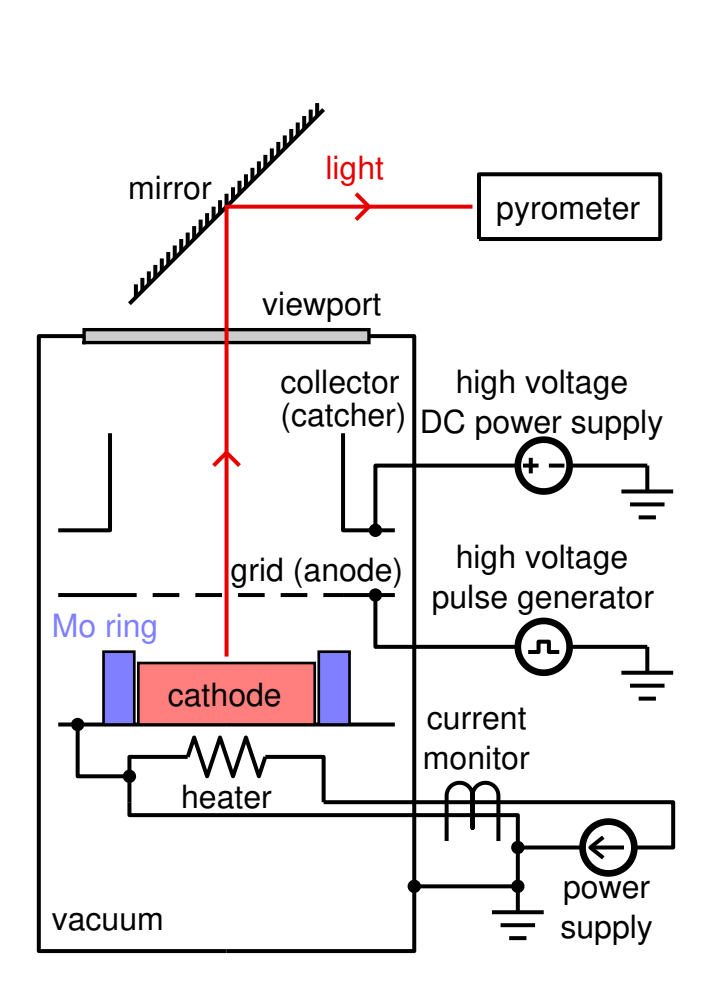


Figure 4.1: Sketch of the closely spaced diode testing vehicle used to measure the thermionic emission current. The rectangle filled with pink is the cathode. The purple rectangles around the cathode represent the molybdenum ring used to shield the side emission.

5 Modeling the emission from real cathodes

This chapter comes from [46], first-authored by me. I am the lead researcher of this topic.

5.1 Introduction

Numerous experimental and computational studies have shown that the microstructure of real W-based cathodes is complex. The tungsten bodies are polycrystalline and porous, and the cathode surfaces are spatially heterogeneous, with the presence of machining marks from the cathode manufacturing process also contributing to the heterogeneity and contributing local field enhancement effects.[7, 47, 48, 49] One of the results of the complex microstructure is that W-based cathodes are spatially heterogeneous with a distribution of grain sizes and many types of exposed surfaces. These surfaces might have varied crystal facets and metal oxide coatings, each with an associated work function value, leading to highly nonuniform emission.[6, 8, 9, 50, 51, 15, 52] The nonuniform nature of thermionic electron emission from polycrystalline W has been observed experimentally by using thermionic electron emission microscopy (ThEEM).[15, 14, 53, 54, 55, 56, 57, 58, 59, 60, 61] In a representative ThEEM image, at a particular temperature, certain grains of the W surface are bright while others remain dark, indicating that some grains are more emissive than others, due to factors such as lower work function, surface topography, etc.

Emission-current-density-versus-temperature, or J-T (Miram) curves and emission-current-density-versus-voltage, or J-V (I-V) curves are commonly used to evaluate the cathode performance. Both the J-T and J-V curves of a cathode can be divided into three regions: temperature-limited (TL) region, full-space-charge-limited (FSCL) region, and the TL-FSCL transition region. The TL region is in the low-temperature end of an J-T curve or the high-voltage end of an J-V curve. Its behavior can be well described with the Richardson–Laue–Dushman equation[19, 20] with Schottky barrier lowering[23]. The FSCL region is in the high-temperature end of a J-T curve or the low-voltage end of a J-V curve. The behavior can be predicted by the Child–Langmuir law[24, 25] and Langmuir and Fry's models[25, 26], including provision for two-dimensional

edge-correction effects[62, 63, 64, 65, 66, 39, 67]. Experimental observations on real thermionic cathodes show that the TL-FSCL region is usually smooth, sometimes referred to as the "roll-off". Despite this seemingly simple observed behavior, it has remained an ongoing challenge to develop a physics-based emission model which is able to accurately predict the behavior of both J–T and J–V curves from polycrystalline cathodes over the entire operational domain of temperature and anode-cathode voltage, and especially challenging to capture the smooth transition between the TL and FSCL regions for real cathodes. Thermionic cathodes are typically operated on the FSCL side near the TL-FSCL transition region, so that the changes in cathode temperature over time do not cause large variations to the emission current and that the emission is stable over the predicted lifetime of the device.

Some empirical descriptions on the smooth TL-FSCL region have been developed, including the empirical Longo-Vaughan equation[33, 34], a continuous Gaussian distribution of work function[21], the work function distribution mathematical treatment of emission data[68], and the practical work function distribution (PWFD)[35]. However, all of these models are based on empirical equations or a priori assumptions that are difficult to justify, such as, the assumption that different work function patches do not interact. Furthermore, these empirical descriptions are not able to reveal the fundamental origin of the smooth behavior of the TL-FSCL transition, thus limiting their usefulness for modeling cathode behavior under different operating conditions.

A number of previous works have studied the interplay of a heterogeneous cathode surface on the resulting thermionic emission, and have sought to connect the smooth TL-FSCL transition to the spatial distribution of work function values. The theory of the anomalous Schottky effect[30] studied the contribution of the patch field effect (electrostatic potential nonuniformity on the cathode surface based on local work function values) and the Schottky barrier lowering effect on the smoothness of the TL-FSCL transition in J - V curves. Studies on space charge effects[39, 67, 31, 32] reveal the contribution of 3-D space charge fields on the smooth transition in J - T curves. However, the TL-FSCL transition behaviors predicted from these two separate sets of studies are sharper than experimental observations, indicating that some physical effects are

missing. There has been no physics-based emission model which can predict the TL-FSCL transition in agreement with experimental results, although Longo and Vaughan speculated[33, 34] that sharper Miram curve knees might be associated with more uniform work function surfaces, or "better" cathodes. Our recent work[37] developed a physics-based model that included the effects of nonuniform thermionic emission, 3-D space charge, patch fields, and Schottky barrier lowering. That work gave a mathematical method to calculate the emission current from a cathode with a spatially heterogeneous work function distribution in a parallel diode, and was able to predict a smooth and gradual TL-FSCL transition comparable with experimental observations by using a checkerboard work function distribution. Those findings were encouraging, and indicated our model may be able to predict the emission of a real cathode, including the smooth TL-FSCL transition, by applying a two-dimensional work function map obtained from the same real cathode.

In this work, we construct a two-dimensional work function map by incorporating the grain orientation via electron backscatter diffraction (EBSD) and the facet-orientation-specific work function values from density functional theory (DFT) calculations. We use this work function map in conjunction with the nonuniform emission model developed in our previous work[37] to predict both the J–T (Miram) and J–V (I–V) curves, including the TL-FSCL transition. Overall, we find semi-quantitative agreement of our predicted results with experimental measurements. This is the first time a physics-based thermionic emission model incorporating heterogeneous surface effects from a work function distribution on a real commercial thermionic cathode has been used to successfully model the experimental emission over a wide domain of temperature and applied voltage.

5.2 Cathode sample

The cathode analyzed in this work is a commercial S-type cathode made by 3M Technical Ceramics. The cathode was made of 80% density W using standard manufacturing methods and impregnated with an oxide mixture of BaO: CaO: $Al_2O_3 = 4:1:1$. The cathode was cylindershaped with a 2.77 mm diameter and 0.97 mm height, as measured after the emission test.

5.3 Microstructure characterization

The cathode surface grain orientation was characterized using electron backscatter diffraction (EBSD) in a FEI Helios G4 Plasma FIB/FESEM/EBSD/EDS workstation after the emission test. The surface of commercial dispenser cathodes is usually rough due to the machining process of cutting the cathode pellets on a lathe. The machining typically produces micrometer-scale ridges, and those differences can be seen in variation in emission properties.[69] Confidence index (CI) values in the EBSD results were used to quantify the likelihood of correct grain orientation labeling.[70] CI standardization, one of the built-in clean-up algorithms in OIM AnalysisTM by EDAX, a software for EBSD analysis, was used to process the raw EBSD data. Pixels with low CI values after applying the CI standardization clean-up procedure were considered as areas where grain orientations were unable to be correctly labeled by EBSD[71] and the surface facet orientation could not be reliably determined. Visual inspection showed that the majority of pixels with CI lower than 0.1 were associated with nonemitting areas, such as rough valleys, depressions, grain boundaries, and pores.[72] Thus, areas with CI < 0.1 were considered as no-emit areas, and the grain orientation of areas with CI \geq 0.1 were considered as recognizable areas. We then used simulations described below to establish a two-dimensional work function map $\phi_{\text{DFT}}(x,y)$ for CI \geq 0.1 areas.

5.4 Density functional theory work function values

Previous density functional theory (DFT) studies have calculated the work functions and surface stabilities of tungsten surfaces with Ba, O, and Ba-O adsorbates of eight different orientations: (001), (011), (111), (210), (211), (221), (310), (311).[8, 9, 52] Auger analysis indicates that the active state for impregnated cathodes can be reproduced by a near monolayer of the stoichiometric Ba-O on the W surface.[51] Only the DFT work function value for the most stable stoichiometric Ba-O adsorption were used to assign to each orientation (Table 5.1). For a high-index orientation (hkl) other than the calculated eight orientations, the nearest neighbor algorithm is used to predict its work function.[73] It was assumed that a facet with an (hkl) orientation had the same work function as the one among the calculated eight orientations with the smallest misorientation with

(hkl) (Fig. 5.1).

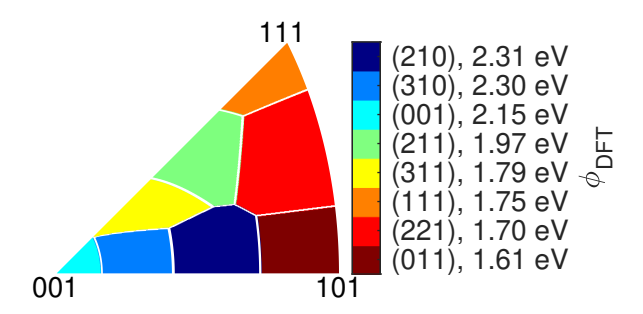


Figure 5.1: Inverse polar figure (IPF) showing how a grain orientation is grouped into one of the eight orientation groups using the nearest neighbor algorithm. The colors indicate the work function values assigned to each orientation group, which are the work function values of the W surface with most stable stoichiometric Ba-O adsorption calculated by density functional theory (DFT).

A few studies have estimated the uncertainty of DFT work function values by comparing DFT results with experimental results. De Waele *et al.*[74] compared the experimental work function values for different surface orientations for a number of metals with the values predicted by the Perdew-Burke-Ernzerhof parametrization of the generalized gradient approximation (PBE-GGA) method. They did a linear fit of DFT values ϕ_{DFT} and experimental values ϕ_{exp} . The result was the equation $\phi_{exp} = \beta_1 \phi_{DFT} + \beta_0$, where the values of the fitted coefficients were $\beta_1 = 0.99 \pm 0.02$ and $\beta_0 = 0.30 \pm 0.09$ (eV). Tran *et al.*[75] also compared their DFT results, ϕ_{DFT} , with experimental values, ϕ_{exp} , on single crystals. They made a single-parameter $\phi_{DFT} = \phi_{exp} - c$ least square fit, where their result was c = 0.30 eV. Both results indicate that DFT work function predictions of metals using GGA-level functionals tend to underestimate the work function values by approximately 0.30 eV, on average, compared with experimental results, and that the error of the estimate is on the scale of tenths of eV even after the linear fit. Due to this known underestimation, we considered the shift between experimental and calculated work function as a fitting parameter in our emission modeling (more details in Section 5.5).

5.5 Emission modeling

It is prohibitively difficult to accurately measure, and thus, to know, the exact anode-cathode distance d at the operating temperatures in our test fixture. Therefore, to better compare the results of the emission model with the experimental results, in this work, we obtained the effective anode-cathode distance d by fitting the FSCL data points with the Child-Langmuir law with the finite temperature correction[25]:

$$J_{\text{FSCL}} = \frac{4\varepsilon_0}{9} \sqrt{\frac{2e}{m}} \frac{(V - V_{\text{m}})^{3/2}}{(d - z_{\text{m}})^2} \frac{9}{8\sqrt{\pi}} \eta^{-3/2} \left(\int_0^{\eta} \frac{d\eta}{\sqrt{\text{erfcx}\sqrt{\eta} - 1 + 2\sqrt{\eta/\pi}}} \right)^2$$
(5.1)

where ε_0 is the vacuum permittivity, e is the elementary charge, m is the electron mass, V is the anode-cathode voltage, d is the anode-cathode distance, $V_{\rm m}$ and $z_{\rm m}$ are the voltage and the location from cathode of the voltage minimum, $\eta = e(V-V_{\rm m})/(k_{\rm B}T)$ where k is the Boltzmann constant and T is the temperature, and erfcx is the scaled complementary error function. Instead of using the as-designed value of the anode-cathode distance, we used the fitted value for the emission model, which we believe is a more accurate value for high temperatures during emission measurements.

In the theory of the Child-Langmuir law with the finite temperature correction on a uniform cathode,[25] the voltage minimum satisfies the Richardson-Laue-Dushman equation: $J = AT^2 \exp\left[-eV_{\rm m}/(k_{\rm B}T)\right]$, while the voltage minimum position $z_{\rm m}=0$ at the TL-FSCL transition. When fitting d using Eq. 5.1, we made the same assumptions: $z_{\rm m}=0$ and $J=AT^2 \exp\left[-eV_{\rm m}/(k_{\rm B}T)\right]$, where J is the experimentally measured emission current density. Here, $A=4\pi mek^2/h^3=120.173\,{\rm A\,cm^{-2}\,K^{-2}}$ is the Richardson constant where h is Planck's constant.

It is not practical to do EBSD on the whole surface of a cathode, so we characterized the grain orientation on a representative area of the cathode surface (more details in Section 5.7), and used periodic boundary conditions on the edges of the work function map, considering that the nonuniform emission model[37] was designed for spatially periodic work function maps. Considering the error in the DFT work function value, we added a constant shift $\Delta \phi$ on the DFT work function values, $\phi_{\text{DFT}}(x,y)$, to get a shifted work function map, $\phi(x,y) = \phi_{\text{DFT}}(x,y) + \Delta \phi$, for the CI ≥ 0.1

areas.

The roughness of the thermionic cathode used in this study was mainly due to the machining and the grain structures. The range of the field enhancement factor values expected from the roughness features of typical thermionic cathodes is usually small, with an estimated upper bounds of 5.[48, 69, 76, 77] Even in the case that the applied electric field is $500\,\mathrm{V/mm}$, the difference in the Schottky barrier lowering between a surface with a field enhancement factor of $\beta=5$ and a perfectly flat surface $\beta=1$ is only $0.033\,\mathrm{eV}$, which will add a negligible enhancement to the thermionic emission, compared with the uncertainty of the DFT work function values. Therefore, for simplicity in our model, we assumed the cathode surface was perfectly flat and neglected field enhancement effects.

The grain orientation of areas with $\text{CI} \geq 0.1$ were considered as recognizable, and a work function map $\phi(x,y) = \phi_{\text{DFT}}(x,y) + \Delta \phi$ was assigned to these areas. By choosing to assign a uniform reference value of zero to the cathode's Fermi energy, the boundary condition of Poisson's equation for each $\text{CI} \geq 0.1$ area was its vacuum level $V(x,y,z=0) = -\phi(x,y)/e$.[37]. Meanwhile, as the majority of CI < 0.1 pixels were associated with nonemitting areas, such as rough valleys, depressions, grain boundaries, and pores,[72] we obtained the boundary conditions, V(x,y,z=0), for the cathode surface's CI < 0.1 areas by solving the 2-D Laplace's equation $\nabla^2 V(x,y) = 0$. For the 2-D boundary value at each edge of a CI < 0.1 area, we used the V value of the adjacent $\text{CI} \geq 0.1$ area. In this way, we obtained the boundary condition of the whole cathode surface, for both $\text{CI} \geq 0.1$ areas and CI < 0.1 areas, which was the input of the nonuniform emission model[37]. There was only one fitting parameter $\Delta \phi$ in this model.

In the model, the potential energy for an electron present in the space within the diode is obtained by solving Poisson's equation, where the charge density is a nonlinear function of the potential energy in the space. The effect of Schottky barrier lowering is included when calculating the potential energy. The patch field effect is naturally included in the non-equipotential boundary condition at the cathode surface V(x,y,z=0), and 3-D Poisson's equation includes the 3-D space charge effect. Therefore, such a nonuniform emission model includes the effects of 3-D space

charge, patch fields, and Schottky barrier lowering, but neglects the effects of the lateral motion of electrons and the quantum effects (e.g., electron tunneling). More information on the physics and specific calculation methodology of our nonuniform emission model can be found in Ref. [37].

5.6 Results

5.6.1 Spatial distribution of work function

We used EBSD to characterize the spatial distribution of grain orientation for a particular cathode after the emission testing was concluded on that cathode sample. We chose this ordering to ensure that our EBSD measurements captured any microstructural evolution that may have occurred during the high temperature activation and emission testing processes. Fig. 5.2a shows the two-dimensional maps of grain orientation of a representative portion of a cathode surface (more details in Section 5.7). The percentage of each orientation group in the map is listed in Table 5.1.

We measured the emission current from a commercial S-type cathode made by 3M Technical Ceramics (Section 5.2) for various anode-cathode voltages and temperatures (Fig. 5.3). The anode-cathode distance was obtained by fitting the 24 data points above 1340 K in Fig. 5.3a using Eq. 5.1, and the result was $d=1.132\,\mathrm{mm}$. As expected, this is very close to the designed value of 1.06 mm. We ascribe the discrepancy between the fitted distance and the designed value to several reasonable factors that include a likely small difference between the designed distance and the actual fabricated distance (at room temperature) as well as the effects of electron optics and thermal expansion. The constant work function shift was obtained by fitting all of the data points in Fig. 5.3a with the nonuniform emission model, and the result was $\Delta\phi=0.176\,\mathrm{eV}$, which indicates that DFT underestimated the work function values compared with the thermionic emission test results. This result is consistent with previous studies on the error of DFT predicted work function values[74, 75] in both the sign and magnitude of the error (underestimation by DFT of approximately 0.3 eV). Fig. 5.2b is the predicted work function map, obtained by applying shifted DFT work function values to the grain orientation map (Fig. 5.2a).

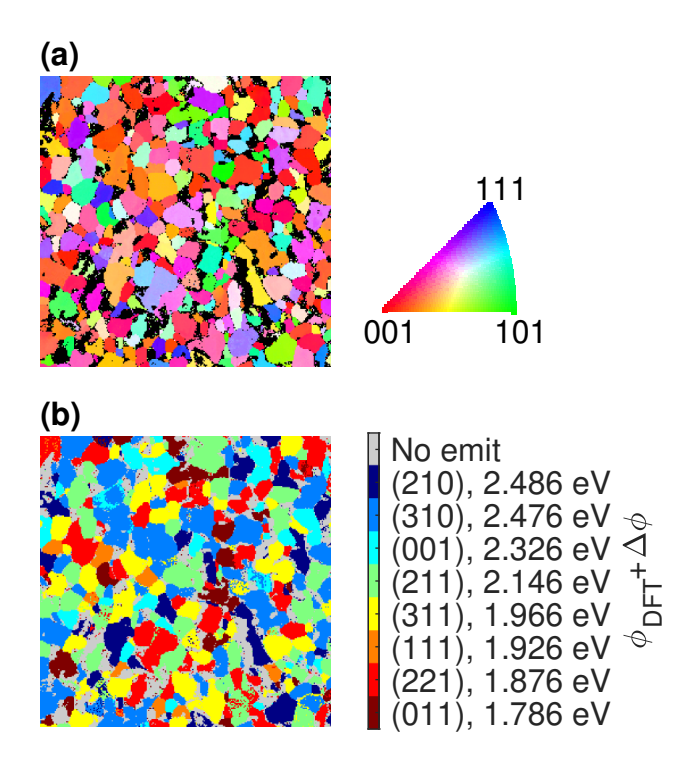


Figure 5.2: (a) Electron backscatter diffraction (EBSD) inverse polar figure (IPF) of a commercial S-type cathode after clean-up. The areas where it is considered that grain orientations are unrecognized by EBSD are plotted in black. (b) Work function map by assigning the density functional theory (DFT) work function value [5] with a shift of $\Delta \phi = 0.176\,\mathrm{eV}$ to the grain orientation map (a) after grouping the orientations into one of the eight orientation groups.

Table 5.1: List of the eight orientations with work function values predicted using density functional theory (DFT). ϕ_{DFT} is the DFT work function value for the most stable stoichiometric Ba-O adsorption for each orientation. $\phi_{DFT} + \Delta \phi$ is the shifted work function value where the shift is $\Delta \phi = 0.176\,\mathrm{eV}$. The "Percentage" column shows the percentage of each orientation group in Fig. 5.2.

$\phi_{\mathrm{DFT}}\left(\mathrm{eV}\right)$	$\phi_{\mathrm{DFT}} + \Delta \phi \ (\mathrm{eV})$	Percentage
2.15	2.326	6.3%
1.61	1.786	5.5%
1.75	1.926	2.3%
2.31	2.486	8.9%
1.97	2.146	14.0%
1.70	1.876	12.7%
2.30	2.476	19.3%
1.79	1.966	13.8%
-	-	17.1%
	2.15 1.61 1.75 2.31 1.97 1.70 2.30	1.61 1.786 1.75 1.926 2.31 2.486 1.97 2.146 1.70 1.876 2.30 2.476

5.6.2 Emission current density

Fig. 5.3 shows the experimental emission data from the S-type cathode and the emission current density predicted by applying the nonuniform emission model [37] to the work function map (Fig. 5.2b). The predicted TL-FSCL transition regions are as smooth as the experimental observations for both the J-T and J-V curves, resulting in semi-quantitative agreement between our model and experimental measurements.

There are only two fitting parameters in our model: the anode-cathode distance $d=1.132\,\mathrm{mm}$ and the constant shift on DFT work function values $\Delta\phi=0.176\,\mathrm{eV}$. The main effect of a different d is to scale up and down the FSCL current, while the effect of a different $\Delta\phi$ is to scale up and down the TL current or shift the TL region to a lower or higher temperature in J-T curves. Using fitted values for these two parameters helps to get a better fit for the TL and FSCL regions, enabling a better comparison on the TL-FSCL transition regions between predicted curves and experimental results. The exact values of both of these fitted parameters have negligible effects on the shape of the TL-FSCL transition region.

The smooth TL-FSCL transition in the predicted curves arises as a natural consequence of the nonuniform emission from the polycrystalline cathode with a nonuniform spatial distribution of work function. Previous studies[39, 67, 31, 32] show that the 3-D space charge effect plays a significant role in making the transition region smooth for a nonuniform cathode. However, when using a work function map for a real cathode derived from DFT and EBSD, a model only considering the 3-D space charge effect predicts a TL-FSCL transition in a Miram curve sharper than experimental results.[31] The nonuniform emission model used in this work[37] includes all of the effects of 3-D space charge, patch fields, and Schottky barrier lowering. This result shows that including all of these effects is required to predict the smooth TL-FSCL transition region in the J-T and J-V curves, not only for the checkerboard model cathode illustrated in[37], but also in a work function map of a real cathode.

The Richardson constant A is an important factor in the Richardson-Laue-Dushman equation. Its theoretical value is $A = 4\pi mek^2/h^3 = 120.173 \,\mathrm{A\,cm^{-2}\,K^{-2}}$. In multiple previous studies, the

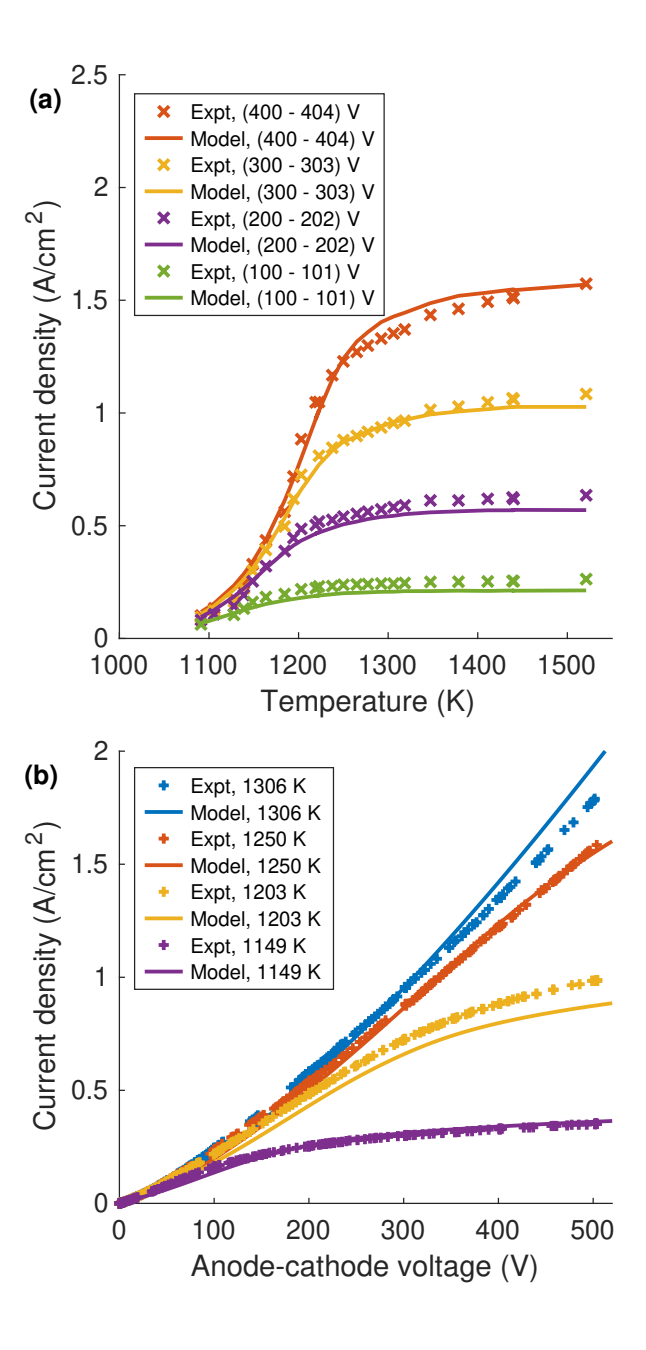


Figure 5.3: Experimental data (× and + symbols) of an S-type cathode compared with the emission current density predicted with nonuniform emission model (lines) at different anode-cathode voltages. (a) J-T curves for different anode-cathode voltages V. The measured V values for the data points of red × symbols are between 400 V and 404 V, $300 \text{ V} \leq V \leq 303 \text{ V}$ for yellow, $200 \text{ V} \leq V \leq 202 \text{ V}$ for purple, and $100 \text{ V} \leq V \leq 101 \text{ V}$ for green. (b) J-V curves at different temperatures.

Richardson constant was experimentally obtained by fitting both the Richardson constant and the effective work function in the Richardson-Laue-Dushman equation to the experimental emission data under the assumption that the cathode is uniform and has a single work function value.[45] It has been observed that, using this method, the experimental values of the Richardson constant differ from the theoretical value, sometimes by many orders of magnitude.[21, 45] However, the Richardson constant does not need to be fit in our model, and is assumed to be fixed to its theoretical value. The agreement between our experimental and predicted J-T and J-V curves indicates that the alteration of the Richardson constant is not needed here. Thus, a key strength of our present model is that knowledge of the fractions of different surface terminations present, their arrangement in 2D space on the surface, and their work functions are all that is required for the nonuniform emission model to provide a physically complete picture of the emission.

5.6.3 Two-dimensional emission map

Fig. 5.4 shows how the calculated emittedssion current density maps change as temperature increases and the emission changes from the temperature-limited (TL) region (Fig. 5.4a), to the transition region (Fig. 5.4b and 5.4c), and finally to the full-space-charge-limited (FSCL) region (Fig. 5.4d). To better illustrate the effects of the patch fields and space charge, we plotted schematic figures of equipotential curves and electric flux lines in the space in front of a low work function patch surrounded by high work function patches in TL, transition, and FSCL regions (Fig. 6.2).

In the TL region (Fig. 5.4a), the space charge effect is negligible, and therefore the low work function patches emit more than the high work function patches. The result that the emission current density varies across different grains due to the difference in their work function values (ϕ) is consistent with experimental thermionic electron emission microscopy (ThEEM) images obtained in the TL region.[15, 14, 53, 54, 55, 56, 57, 58, 59, 60, 61]

As the schematic figures show, in the TL region (Fig. 6.2a), the space charge effect is negligible, so the electrostatic potential in this case is close to the solution of the 3-D Laplace's equation $\nabla^2 V(x,y,z) = 0$. The nonuniform boundary condition at the cathode surface V(x,y,z=0) = 0.

 $-\phi(x,y)/e$ introduces additional electric fields between different work function patches besides the applied electric field between the anode and the cathode. Therefore, the equipotential contours and electric flux lines are bent in the space close to the patch boundaries. Such additional electric fields between different patches are referred to as the patch fields. The patch fields lead to a voltage minimum (potential depression, also called as the virtual cathode) occurring a short distance above the edges of the strongly-emitting low- ϕ patch. This causes the local emission current density J(x,y) at the edge of low- ϕ patches to be smaller than the center of the patches (Fig. 5.4a).[12, 13, 30] In the transition region (Fig. 5.4b), this patch field effect continues to depress low work function patches' edge currents relative to their center currents, even though a potential depression begins to form above the patch center due to the space charge effect (Fig. 6.2b). Note that the reduced edge emission of low work function patches due to patch fields contrasts with enhanced edge emission on a cathode surface with nonuniform emission but without patch field effects. In the latter case, the edges of high-emitting patches emit more than the center of the patches due to the lower space charge in front of their neighboring low-emitting patches.[64, 65, 67]

In the transition and FSCL regions (Fig. 6.2b, 6.2c, and 6.2d), the more strongly-emitting, low- ϕ patches have more significant space charge effects than the less-emitting, high- ϕ patches. As observed in Fig. 6b and 6c, the strongly-emitting, low- ϕ patches develop voltage minima above their surfaces at these transition region temperatures. This space charge effect limits the emission from the low- ϕ patches while the emission from the high- ϕ patches continues to increase without such limitation. This 3D space charge effect causes the emission to become increasingly more spatially uniform as the temperature increases from the transition region to the FSCL region (Fig. 5.4b, 5.4c, and 5.4d).

In our nonuniform emission model, even though electrons are restricted along the cathodeanode direction with no lateral momentum, our model is able to predict the trend of the change in the emission nonuniformity as temperature changes. Such a trend has also been observed in experiments[78, 79] and is consistent with some previous computational studies[39, 67, 31, 32].

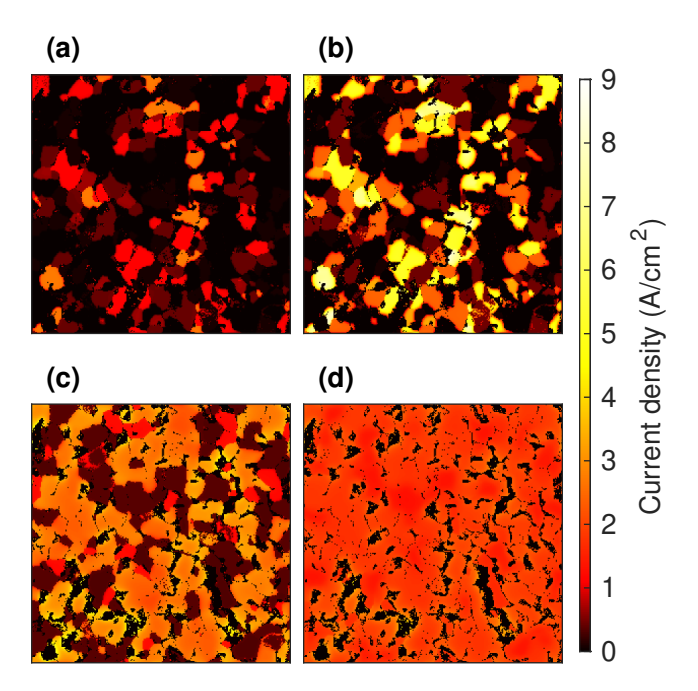


Figure 5.4: Emission current density maps predicted using nonuniform emission model for a cathode with work function map as Fig. 5.2b at anode-cathode voltage $V=400\,\mathrm{V}$ and distance $d=1.132\,\mathrm{mm}$, at different temperatures: (a) TL region: temperature $T=1149\,\mathrm{K}$, average emission current density $J=0.340\,\mathrm{A/cm^2}$, (b) transition region: $1250\,\mathrm{K}$, $J=1.234\,\mathrm{A/cm^2}$, (c) transition region but with an average emission current density close to the full-space-charge-limited (FSCL) value: $1411\,\mathrm{K}$, $J=1.525\,\mathrm{A/cm^2}$, (d) FSCL region: $1521\,\mathrm{K}$, $J=1.552\,\mathrm{A/cm^2}$.

5.7 Sensitivity analysis and sources of error

It is computationally expensive to simulate large areas (for example, 0.1 mm² or larger) with the nonuniform emission model and time-consuming to characterize the grain orientation of a large area where there are a large number of grains. The computational cost is significantly increased in beam optics simulations where millions of time steps are typically used.[80] To determine the representativeness of the statistics of the surface facets and ascertain the relationship between the uncertainty of the predicted emission current and the size of the work function map, we characterized a total of 9 EBSD maps on different regions of the S-type cathode, for a total examined area of 0.15 mm², and calculated the resulting emission current density as a function of the examined area of the cathode surface.

To evaluate the effect of the uncertainty in the work function values to the predicted emission current density, we calculated the emission current density from a work function map by applying $\phi(hkl) = \phi_{\rm DFT}(hkl) + \Delta\phi(hkl)$ to the grain orientation map in Fig. 5.2a, where the (hkl) is one of the eight grain orientations assigned with DFT work function values, and the work function shift for the eight grain orientations $\Delta\phi(hkl)$ are assumed to be independent and identically distributed (i.i.d.) following the normal distribution $\Delta\phi(hkl) \sim N(0.176\,{\rm eV},\sigma_{\rm DFT}^2)$, where the standard deviation $\sigma_{\rm DFT}$ represents a phenomenological error in our DFT measurements. We have generated 2500 random work function maps for each $\sigma_{\rm DFT}$ value and calculated the variability of their emission current densities.

Fig. 5.5 shows the variability of the values of the emission current density for different submap sizes (Fig. 5.5a) and different uncertainties of work function values (Fig. 5.5b) at a condition for the TL-FSCL transition region. Fig. 5.5a shows how the prediction of the emission current density becomes more precise as the size of the submap increases, which indicates that model users may determine the submap size to use according to their desired precision in the prediction. Fig. 5.5b estimates the uncertainty in the predicted emission current density as a function of the uncertainty in the work function values. Previous studies[74, 75] estimated that the error of the DFT work function values is on the scale of tenths of eV. Our results show that even in the extreme case

that the DFT work function values have an uncertainty of $0.4\,\mathrm{eV}$, the median (the red line in the box in Fig. 5.5b) is $1.29\,\mathrm{A/cm^2}$, close to $1.23\,\mathrm{A/cm^2}$, which was the result for the baseline case ($\phi = \phi_\mathrm{DFT} + 0.176\,\mathrm{eV}$, Fig. 5.3 and 5.4b). In the $\phi_\mathrm{DFT} = 0.4\,\mathrm{eV}$ results, the first quartile (the lower edge of the box) is $Q_1 = 1.11\,\mathrm{A/cm^2}$ while the third quartile (the upper edge) is $Q_3 = 1.41\,\mathrm{A/cm^2}$, and the interquartile range is $IQR = Q_3 - Q_1 = 0.29\,\mathrm{A/cm^2}$. Such a dispersion is smaller than using a $32\,\mu\mathrm{m} \times 32\,\mu\mathrm{m}$ submap, which has $IQR = 0.37\,\mathrm{A/cm^2}$, indicating a robustly predicted average current density even for the higher end of DFT work function uncertainty values.

Other possible causes of the error in the predicted emission current density include the measurement error in temperature values, the dependence of the work function value on temperature due to different stable arrangements of Ba-O surface species at different temperatures, and the dependence of the anode-cathode distance on temperature due to thermal expansion. The assumptions in the nonuniform emission model[37] may also contribute to the error in the predicted emission, which include the assumption of a perfectly flat cathode surface in an infinite parallel diode, neglecting the lateral motion of the electrons, and neglecting the quantum effects. While it is beyond the scope of the present work to perform an in-depth investigation of the role of each of these sources of error, we find it very encouraging that the results in Fig. 5.3 illustrate that our model shows near quantitative agreement with experiment over a wide range of temperatures and anodecathode voltages. This strong agreement with experiment suggests that while many sources of uncertainty in our model exist, they likely play a minor role in the resulting emission compared with the microstructural features of the cathode, including the fractions of each surface present, their size and spatial distribution, and the relative work functions of grains comprising the cathode surface.

5.8 Conclusions and Outlook

Our nonuniform emission model can predict two-dimensional maps of emission current density and therefore the average emission current densities at different temperatures and anode-cathode voltages based on a two-dimensional work function map derived by DFT calculations and mi-

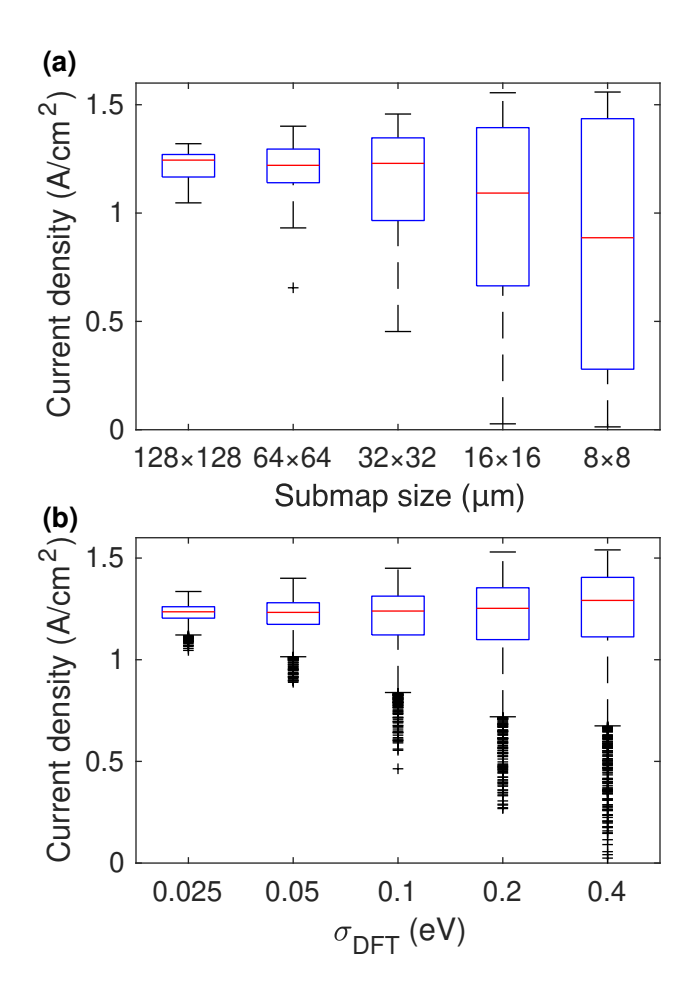


Figure 5.5: Boxplots showing the variability of the emission current density predicted (a) from the submaps of different characterized area sizes at temperature $T=1250\,\mathrm{K}$, anode-cathode voltage $V=400\,\mathrm{V}$ and distance $d=1.132\,\mathrm{mm}$, (b) from a work function map by applying $\phi(hkl)=\phi_{\mathrm{DFT}}(hkl)+\Delta\phi(hkl)$ to the grain orientation map in Fig. 5.2a, where the shift values are independent and identically distributed (i.i.d.) following the normal distribution $\Delta\phi(hkl)\sim N(0.176\,\mathrm{eV},\sigma_{\mathrm{DFT}}^2)$. In a boxplot, the red line in the box indicates the median value. The lower edge of the box is the first quartile (Q_1 or 25th percentile). The upper edge is the third quartile (Q_3 or 75th percentile). The interquartile range (IQR) is defined as IQR = Q_3-Q_1 . Data points larger than $Q_3+1.5\mathrm{IQR}$ or smaller than $Q_1-1.5\mathrm{IQR}$ are considered as outliers and plotted individually using the + symbols. The whiskers extend to the most extreme data points not considered to be outliers.

crostructure characterization. Importantly, the predicted J-T and J-V curves are in semiquantitative agreement with experimental results, including the nature of the TL-FSCL transition, which shows the same shape as experiments. There are only two fitting parameters in our model: the anode-voltage distance and a constant shift on the DFT work function values. The effect of these two fitting parameters on the shape of the TL-FSCL transition is negligible. Our model is the first of its kind to use a physics-based modeling method coupled with experimental characterization to reproduce experimental emission data, and illustrates that it is not necessary to use an empirical equation such as the Longo-Vaughan equation or to assume a continuous work function distribution. A key result of this work is that a smooth TL-FSCL transition region is a natural consequence of the physics of the nonuniform emission from a spatial distribution work function map when the effects of 3-D space charge, patch fields, and Schottky barrier lowering are included.

The present findings provide both a robust physics-based approach to predict the emission current from any polycrystalline cathode for which the surface grain orientations and work functions are known, and a means to understand how the cathode microstructure and the underlying work functions couple to the expected emission behavior. The present "forward" model starts from cathode work function distributions and predicts J-T and J-V curves. In the future, it may be possible to to create an "inverse" model where one starts from experimentally measured J-T and/or J-V curves and predicts an effective cathode work function arrangement and associated microsctructure consistent with the measured emission. Such an approach may be an effective method to better understand the coupling of cathode microstructure with the measured emission of new cathodes. Such a method would provide a powerful tool for understanding the expected emission behavior of new cathodes, as conducting an emission test on a new cathode is less time-consuming than a full suite of microstructure and work function studies, e.g., using EBSD characterization and DFT calculations. The results in this work can also be used as input for higher-level simulation codes like MICHELLE[80] to improve the modeling of cathodes in electron gun fixtures, better informing device design and enabling deeper insight into the physical factors governing heterogeneous emission from thermionic cathodes.

6 Physical factors governing the shape of Miram curve

This chapter comes from [81], first-authored by me. I am the lead researcher of this topic.

6.1 Introduction

J-T curves normalized by the extrapolated full-space-charge-limited emission current density J_{FSCL} are referred to as Miram curves, named after George Miram.[82] Miram (or J-T) curves are widely used as a figure of merit to evaluate the cathode performance. Experimental observations show there is a smooth transition, called the "roll off" or Miram curve knee, between the exponentially growing (temperature-limited or TL) region and the saturated emission current (full-space-charge-limited or FSCL) region. The shape characterizing the Miram curve knee is important as thermionic cathodes are almost always operated at a temperature slightly above the Miram curve knee. For VEDs used in space applications, the operating point may be slightly above the knee temperature to realize stable cathode operation at the lowest temperature, thus maximizing cathode lifetime and reducing the input power required to keep the cathode at high temperature. For non-space applications, a higher temperature may be used in order to maintain space charge limited emission and mitigate potential fluctuations in the emitted current density that may occur if the cathode enters the temperature-limited emission region. [31, 83] Thus, knowledge of the shape of the Miram curve knee region, including the smoothness, the temperature, and the flatness of the saturated emission current density can inform desired operational parameters of VEDs using thermionic cathodes.

Our recent work[37] developed a physics-based model of nonuniform thermionic emission that includes the effects of space charge, patch fields, and Schottky barrier lowering, giving a mathematical method to calculate the emission current from a cathode with a spatially heterogeneous work function distribution in a parallel diode. This model predicts a smooth Miram curve knee for a model cathode surface consisting of a 2-D checkerboard work function distribution. The results of this model reveal that the smoothness of the Miram curve knee arises as a natural consequence

of the physics of nonuniform thermionic emission, and that the space charge and patch field effects have more significant impact on smoothing the Miram curve knee than the effect of Schottky barrier lowering. Further study[46] showed that when a 2-D work function distribution obtained from a commercial tungsten dispenser cathode is used with this nonuniform emission model, the model is able to predict the J-T and J-V emission curves in near quantitative agreement with experimental data, and accurately predicts the shape of the Miram curve knee.

Our previously published work[37] on the nonuniform emission model successfully included the predictions of key characteristics of the Miram curve, including the smooth knee, but it did not include a detailed examination of the different physical factors connecting the effects of space charge and patch fields and their relative impact on the shape of the Miram curve knee. In this work, we use our nonuniform emission model to further study the effects of space charge and patch fields on the shape of the Miram curve knee, with the goal of understanding which physical parameters have the most significant impact on the shape of the knee, and how the typical ranges of the values of these parameters impact the knee. Knowledge of how the surface microstructure, including the work function values and the emitting patch area sizes affect the shape of the Miram curve knee would provide new understanding of cathode materials design and engineering. Similarly, incorporating the effects of diode geometry and anode-cathode voltage could improve the design of electron gun fixtures used in VEDs. This work also provides new insights in the analysis of experimental Miram curves, which are useful for developing and understanding the performance of novel thermionic cathodes using new materials.

6.2 Zebra crossing work function distribution

Checkerboard work function distributions[42, 12, 43, 13, 32, 39, 37] and equal-width periodic stripes (or "zebra crossing") work function distributions[31, 32, 30, 29] are two model work function distributions used in previous studies of nonuniform thermionic emission. As illustrated in[32], many of the fundamental properties of electron emission from the two-dimensional checkerboard distribution are observable with the simpler, one-dimensional, zebra-crossing distribution.

Therefore, in this work we use the zebra crossing surface model to analyze the effects of space charge and patch fields on the shape of Miram curve.

Fig. 6.1 illustrates the zebra crossing model of nonuniform work function distribution on a surface. In this work, we let the x-axis run along the surface of the cathode, perpendicular to the patch edges, and the y-axis run along the cathode-anode direction, i.e., the direction of electron emission away from the surface. The cathode is set to be at y=0, while the anode at y=d. Mathematically, the work function as a function of surface position is:

$$\phi(x) = \begin{cases} \phi_1, & (2N-1)a < x < 2Na \\ \phi_2, & 2Na < x < (2N+1)a \end{cases}$$
(6.1)

where $\phi_1 > \phi_2 > 0$, $N = 0, \pm 1, \pm 2,...$ is any integer.

anode:
$$y = d$$

$$x = -3a \quad -2a \quad -a \quad 0 \quad a \quad 2a \quad 3a$$
...
$$\phi_1 \quad \phi_2 \quad \phi_1 \quad \phi_2 \quad \phi_1 \quad \phi_2 \quad ...$$

Figure 6.1: Model heterogeneous emission surface characterized as a "zebra crossing" spatial distribution of work function in a laterally infinite parallel diode.

6.3 Effects of patch fields and space charge

To better illustrate the effects of the patch fields and space charge, we plotted schematic figures of equipotential curves and electric flux lines in the space in front of a low work function patch surrounded by high work function patches in TL, transition, and FSCL regions (Fig. 6.2).

In the TL region (Fig. 6.2a), the space charge effect is negligible, and therefore the low work function patches emit more than the high work function patches. The result that the emission current density varies across different grains due to the difference in their work function values (ϕ) is consistent with experimental thermionic electron emission microscopy (ThEEM) images obtained in the TL region.[15, 14, 53, 54, 55, 56, 57, 58, 59, 60, 61]

As the schematic figures show, in the TL region (Fig. 6.2a), the space charge effect is negligible, so the electrostatic potential in this case is close to the solution of the 3-D Laplace's equation $\nabla^2 V(x,y,z) = 0$. The nonuniform boundary condition at the cathode surface $V(x,y,z=0) = -\phi(x,y)/e$ introduces additional electric fields between different work function patches besides the applied electric field between the anode and the cathode. Therefore, the equipotential contours and electric flux lines are bent in the space close to the patch boundaries. Such additional electric fields between different patches are referred to as the patch fields. The patch fields lead to a voltage minimum (potential depression, also called as the virtual cathode) occurring a short distance above the edges of the strongly-emitting low- ϕ patch. This causes the local emission current density J(x,y) at the edge of low- ϕ patches to be smaller than the center of the patches.[12, 13, 30]

In the transition region (Fig. 6.2b), this patch field effect continues to depress low work function patches' edge currents relative to their center currents, even though a potential depression begins to form above the patch center due to the space charge effect. Note that the reduced edge emission of low work function patches due to patch fields contrasts with enhanced edge emission on a cathode surface with nonuniform emission but without patch field effects. In the latter case, the edges of high-emitting patches emit more than the center of the patches due to the lower space charge in front of their neighboring low-emitting patches.[64, 65, 67]

In the transition and FSCL regions (Fig. 6.2b, 6.2c, and 6.2d), the more strongly-emitting, low- ϕ patches have more significant space charge effects than the less-emitting, high- ϕ patches. As observed in Fig. 6b and 6c, the strongly-emitting, low- ϕ patches develop voltage minima above their surfaces at these transition region temperatures. This space charge effect limits the emission from the low- ϕ patches while the emission from the high- ϕ patches continues to increase without such limitation. This 3D space charge effect causes the emission to become increasingly more spatially uniform as the temperature increases from the transition region to the FSCL region.

In our nonuniform emission model, even though electrons are restricted along the cathodeanode direction with no lateral momentum, our model is able to predict the trend of the change in the emission nonuniformity as temperature changes. Such a trend has also been observed in experiments[78, 79] and is consistent with some previous computational studies[39, 67, 31, 32].

6.4 Quantifying the shape of Miram curve knee

We define the TL-FSCL intersection temperature T_i as the intersection temperature of the separate extrapolations of temperature-limited (TL) J_{TL} and full-space-charge-limited (FSCL) J_{FSCL} curves (Fig. 2):

$$J_{\rm TL}(T_{\rm i}) = J_{\rm FSCL}(T_{\rm i}) \tag{6.2}$$

As Fig. 6.3 shows, much of a Miram curve knee may be observed at temperatures greater than the TL-FSCL intersection temperature T_i .

In this work, we use an area-averaged application of the Richardson-Laue-Dushman (RLD) equation to estimate the TL extrapolation. For the zebra crossing work function distribution with equal widths for the two work function stripes (Fig. 6.1), the TL extrapolation equation is

$$J_{\rm TL} = \frac{1}{2} \left[AT^2 \exp\left(-\frac{\phi_1}{k_{\rm B}T}\right) + AT^2 \exp\left(-\frac{\phi_2}{k_{\rm B}T}\right) \right]$$
 (6.3)

where T is the temperature, $k_{\rm B}$ is the Boltzmann constant, and the Richardson constant $A=4\pi mek_{\rm B}^2/h^3$ where h is the Planck constant. The FSCL extrapolation can be estimated using the Child-Langmuir law with finite temperature correction (CLT). The equation at the TL-FSCL intersection temperature $T_{\rm i}$ for a uniform cathode with a single cathode work function value $\phi_{\rm K}$ is:[25, 46]

$$J_{\text{CLT}} = \frac{4\varepsilon_0}{9} \sqrt{\frac{2e}{m}} \frac{V_{\text{AK}}^{3/2}}{d^2} \frac{9}{8\sqrt{\pi}} \eta^{-3/2} \left(\int_0^{\eta} \frac{d\eta}{\sqrt{\text{erfcx}\sqrt{\eta} - 1 + 2\sqrt{\eta/\pi}}} \right)^2$$
(6.4)

where ε_0 is the vacuum permittivity, e is the elementary charge, m is the electron mass, $V_{\rm AK} = V_{\rm applied} - \phi_{\rm A}/e + \phi_{\rm K}/e$ is the difference of the electric potential of the vacuum level between the anode surface and cathode surface, $V_{\rm applied}$ is the applied voltage between the anode and the cathode as measured in experiments, $\phi_{\rm A}$ is the anode work function, $\phi_{\rm K}$ is the cathode work function,

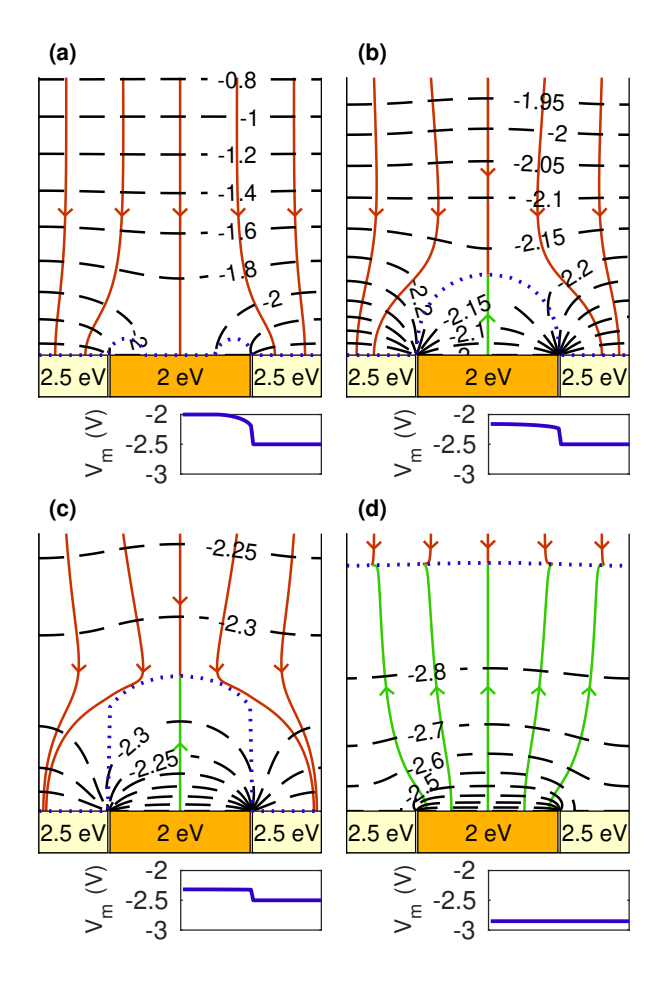


Figure 6.2: Schematic figures illustrating the effects of patch fields and 3-D space charge in different regions: (a) temperature-limited (TL) region, (b) transition region, (c) transition region with an average emission current density close to full-space-charge-limited (FSCL) value, and (d) FSCL region. The anode (not shown in the figures) is far away onabove the top of each subfigure, and the cathode is on the bottom of each subfigure, with a low work function patch (2eV) surrounded by high work function patches (2.5 eV). Dashed black curves are the equipotential curveontours of the electrostatic potential (unit: V). The red and green solid curves are the electric flux lines. The red ones are for the electric flux lines starting from the anode while the green ones for those starting from the cathode. The dotted violet curves indicate the position of voltage minimum $z_m(x,y)$ (position of the virtual cathode). The plots beneath each subfigure (solid violet curves) show the value of the voltage minimum in front of different location of the cathode surface $V_m(x,y)$. The value of $V_m(x,y)$ on the left half (not plotted) is symmetric to the right half. The local emission current density is $J(x,y) = AT^2 \exp\left[-eV_m/(k_BT)\right]$.

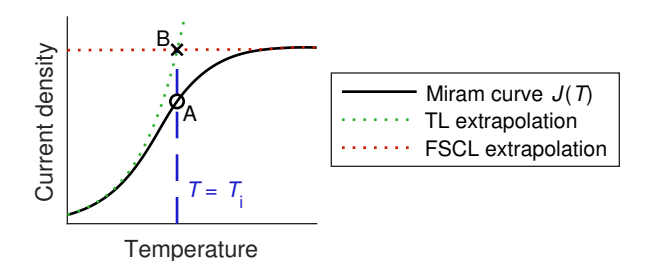


Figure 6.3: Schematic plot illustrating the definition of the TL-FSCL intersection temperature $T_{\rm i}$ (dashed blue line) and the normalized intersection emission parameter α . In this plot, $\alpha = J(A)/J(B)$. The solid black curve is the Miram curve J(T). The dotted red curve is the full-space-charge-limited (FSCL) extrapolation $J_{\rm FSCL}$. The dotted green curve is the temperature-limited (TL) extrapolation $J_{\rm TL}$.

 $\eta = eV_{\rm AK}/(k_{\rm B}T)$, and erfcx is the scaled complementary error function.

For a zebra crossing cathode, we average J_{CLT} over the cathode surface to estimate the FSCL extrapolation J_{FSCL} :

$$J_{\text{FSCL}} = \frac{1}{2} \left[J_{\text{CLT}} |_{\phi_{\text{K}} = \phi_1} + J_{\text{CLT}} |_{\phi_{\text{K}} = \phi_2} \right]$$
 (6.5)

To quantify the impact of the space charge and patch field effects on the emission current density at the TL-FSCL intersection temperature T_i , we define and use the intersection-temperature emission normalized by the FSCL current parameter (Fig. 6.3):

$$\alpha = \frac{J(T_{\rm i})}{J_{\rm TL}(T_{\rm i})} = \frac{J(T_{\rm i})}{J_{\rm FSCL}(T_{\rm i})} = \frac{J(A)}{J(B)}$$

$$(6.6)$$

A high α value represents good cathode performance and a Miram curve with a sharp knee at a low temperature and a flat saturated emission current.

Our previous study on nonuniform emission[37] indicated that space charge and patch fields have a significant impact on the shape of the Miram curve knee. Considering the definition of the normalized emission parameter (Eq. 6.6), we here develop complementary, limiting-case analytic models to separately study the effects: a study of the space charge effect to analyze $J(T)/J_{\rm FSCL}(T)$ and a study of the patch field effect for $J(T)/J_{\rm TL}(T)$.

6.5 Space charge effect

Previous studies on 2-D and 3-D space charge[31, 32] illustrate its effects on the emission current. Seminal work from Lau developed a simple theory for the 2-D Child-Langmuir law.[63] We generalize this 2-D Child-Langmuir law to a cathode with nonuniform emission. In this generalized theory, we make some assumptions as below.

Assumption 1 (same as in Lau's work[63]): The y-axis component of the electric field at $(x_0, 0)$ is

$$E_{y}(x,0) = -\frac{\bar{V}_{AK}}{d} + G \int_{0}^{d} dy' \int_{-\infty}^{+\infty} dx' \frac{\rho(x',y')y'}{2\pi\varepsilon_{0} \left[(x'-x)^{2} + y'^{2} \right]}$$
(6.7)

where G is a constant multiplication factor to account for the contributions due to the image charge. For a zebra crossing model (Fig. 6.1), the averaged electric potential difference between the anode and cathode surfaces is $\bar{V}_{AK} = V_{applied} - \phi_A/e + (\phi_1 + \phi_2)/(2e)$.

To solve for the value of G, we use the 1-D Child-Langmuir (CL) theory at zero temperature for a uniform cathode. In the space-charge-limited region, $E_v(x,0) = 0$, and

$$\rho(x,y) = J_{\rm CL} \left(\frac{d}{y}\right)^{2/3} \sqrt{\frac{m}{2e\bar{V}_{\rm AK}}}$$
(6.8)

where the Child-Langmuir (CL) current density

$$J_{\rm CLT} = \frac{4\varepsilon_0}{9} \sqrt{\frac{2e}{m}} \frac{\bar{V}_{\rm AK}^{3/2}}{d^2}$$
 (6.9)

Solving Eq. 6.7, 6.8, 6.9, we get G = 3/2.

Assumption 2: The charge density has the same functional form as the Child-Langmuir law (Eq. 6.8) but replacing J_{CL} with J(x):

$$\rho(x,y) = J(x) \left(\frac{d}{y}\right)^{2/3} \sqrt{\frac{m}{2e\bar{V}_{AK}}}$$
(6.10)

We make this assumption because we are interested in the knee behavior where the emission current is close to J_{FSCL} and the charge density $\rho(x,y)$ is close to the Child-Langmuir law case.

Assumption 3: For the zebra crossing case, we assume:

- 1. The local emission current density over the ϕ_1 patch is spatially uniform: $J(x) = J_1$, for 2Na a < x < 2Na where N is any integer.
- 2. The ϕ_1 patch emits in the temperature-limited (TL) region when the electric field at the center of the ϕ_1 patch surface is negative, $E_{1y} = E_y(2Na a/2, 0) < 0$.
- 3. The space-charge-limited (SCL) emission current density is also spatially uniform over the ϕ_1 patch, denoted as J_{1SCL} . which is determined by the equation $E_{1y} = 0$.
- 4. The emission current density of the ϕ_1 patch is $J_1 = \min\{J_{1TL}, J_{1SCL}\}$.
- 5. The four items above also apply for the ϕ_2 patch.

Assumption 4 : As $\phi_1 > \phi_2 > 0$, the TL current densities have a relation $J_{2\text{TL}} > J_{1\text{TL}} > 0$, so the high work function patch (ϕ_1) will reach SCL at a temperature higher than the low work function patch (ϕ_2) . It is assumed that the SCL current density for the high work function patch is equal to the 1-D Child-Langmuir theory $J_{1\text{SCL}} = J_{\text{CL}}$ while $J_{2\text{SCL}}$ may be larger than J_{CL} in certain temperatures. This assumption is in agreement with the findings in previous studies[31, 32][5], [13].

Under these assumptions, the electric field at the center of the low work function patch (ϕ_2) is:

$$E_{2y} = \frac{V_{AK}}{d} \left(\frac{J_1}{J_{CL}} + \frac{J_2 - J_1}{J_{CL}} f - 1 \right)$$
 (6.11)

where f is a function of only a/d:

$$f\left(\frac{a}{d}\right) = \frac{1}{3\pi} \int_0^1 d\tilde{y} \sum_{N=-\infty}^{+\infty} \int_{(2N-1/2)a/d}^{(2N+1/2)a/d} \frac{\tilde{y}^{1/3}}{\tilde{x}^2 + \tilde{y}^2} d\tilde{x}$$
 (6.12)

where the symbols with tildes are normalized coordinates $\tilde{x} = x/d$, $\tilde{y} = y/d$.

Letting $E_{2y} = 0$, we can solve for the space-charge-limited (SCL) current density of the ϕ_2 patch: $J_{2SCL} = J_1 + (J_C L - J_1)/f$. Therefore, we can predict the average emission current density for the zebra crossing cathode:

- 1. Temperature-limited (TL) region $J_{1TL} < J_{2TL} < J_{2SCL}$: Neither the ϕ_1 patch nor the ϕ_2 patch reaches SCL. The average current density of the cathode is $J = (J_{1TL} + J_{2TL})/2$.
- 2. Full-space-charge-limited (FSCL) region $J_{2TL} > J_{1TL} > J_{1SCL} = J_{CL}$: Both the ϕ_1 and ϕ_2 patches are SCL, so $J = (J_{1SCL} + J_{2SCL})/2 = J_{CL}$.
- 3. TL-FSCL transition region (i.e., the location of the Miram curve knee) $J_{2\text{TL}} > J_{2\text{SCL}}$ but $J_{1\text{TL}} < J_{1\text{SCL}}$: The low work function patch (ϕ_2) is space-charge-limited (SCL) while the high work function patch (ϕ_1) is still not SCL, so

$$J = \frac{1}{2} (J_{1TL} + J_{2SCL}) = J_{CL} - (J_{CL} - J_{1TL}) \frac{2f - 1}{2f}$$

In particular, at the TL-FSCL intersection temperature T_i , we assume that the temperature satisfies the condition:

$$J_{\rm CL} = J_{\rm TL} = \frac{1}{2} \left[A T_{\rm i}^2 \exp\left(-\frac{\phi_1}{k_{\rm B} T_{\rm i}}\right) + A T_{\rm i}^2 \exp\left(-\frac{\phi_2}{k_{\rm B} T_{\rm i}}\right) \right]$$
(6.13)

The normalized intersection emission restricted by the space charge effect is

$$\alpha_{\rm SC} = \frac{J(T_{\rm i})}{J_{\rm CL}} = 1 - \frac{2f - 1}{2f} \tanh \frac{\phi_1 - \phi_2}{2k_{\rm B}T_{\rm i}}$$
 (6.14)

which only depends on two parameters: (1) the normalized work function difference $(\phi_1 - \phi_2)/(k_B T_i)$ and (2) the patch-diode size ratio a/d (cf. Eq. 6.12: f only depends on a/d).

6.6 Patch field effect

We assume the additional electric potential due to the patch field effect satisfies $\nabla^2 V_{\rm PF}(x,y)=0$, with the boundary condition for the cathode surface $V_{\rm PF}(x,0)=-\phi(x)/e$. We also assume that the anode-cathode distance is much larger than the patch width $d\gg a$, so use $E_y(x,+\infty)=0$ as the boundary condition for the anode side. In this section, we adopt an approximate linear potential assumption, i.e., $\partial V_{\rm linear}/\partial y=-E_0$, where $E_0\leq 0$ is a uniform electric field, to estimate the effects of the applied voltage and the space charge on the electric potential. Under these assumptions, the electric potential is $V=V_{\rm PF}+V_{\rm linear}=V_{\rm PF}-E_0y$. Considering the periodicity and the symmetry of this problem, here we only show the results in -a/2 < x < a/2:

$$V(x,y) = -\frac{\phi_1 + \phi_2}{2e} + \frac{\phi_1 - \phi_2}{e} p(x,y,\beta_E)$$
 (6.15)

where the field ratio

$$\beta_E = \frac{E_{\text{patch}}}{-E_0} = \frac{\phi_1 - \phi_2}{-eaE_0} \tag{6.16}$$

and the parameter

$$p(x, y, \beta_E) = \frac{\ddot{y}}{\pi \beta_E} + \frac{i}{\pi} \left(\operatorname{arctanh} e^{-i \ddot{x} - \ddot{y}} - \operatorname{arctanh} e^{i \ddot{x} - \ddot{y}} \right)$$
(6.17)

where the symbols with breves are normalized coordinates $\check{x} = \pi x/a$, $\check{y} = \pi y/a$, and i is the imaginary unit.

The voltage minimum is

$$V_{\mathrm{m}}(x) = \min_{y} V(x, y) = V(x, y_{\mathrm{m}}(x))$$

where the location of the voltage minimum $y_m(x)$ satisfies

$$\cosh \tilde{\mathbf{y}}_{\mathbf{m}}(x) = \frac{\beta_E \sin \tilde{\mathbf{x}}}{2} + \sqrt{1 + \left[\left(\frac{\beta_E}{2} \right)^2 - 1 \right] \sin^2 \tilde{\mathbf{x}}}$$
 (6.18)

for $0 < \breve{x} < \min \{\pi/2, \arcsin \beta_E\}$, and $y_m(x) = 0$ for elsewhere.

For a given cathode surface location x, the location of the voltage minimum $y_m(x)$ only depends on the field ratio β_E . Therefore, for a given x, the parameter $p(x,y,\beta_E)$ in Eq. 6.17 also only depends on β_E .

The local emission current density follows the RLD equation $J(x) = AT^2 \exp\left[eV_{\rm m}(x)/(k_{\rm B}T)\right]$. The cathode-averaged emission current density J can be obtained by averaging J(x) over the cathode surface. The ratio of the average emission current density J to the TL extrapolation $J_{\rm TL}$ (Eq. 6.3) is:

$$\frac{J}{J_{\text{TL}}} = \frac{\frac{1}{\pi} \int_{-\pi/2}^{\pi/2} AT^2 \exp\left[\frac{eV_{\text{m}}(x)}{k_{\text{B}}T}\right] d\breve{x}}{\frac{1}{2} \left[AT^2 \exp\left(-\frac{\phi_1}{k_{\text{B}}T}\right) + AT^2 \exp\left(-\frac{\phi_2}{k_{\text{B}}T}\right)\right]} = \frac{\frac{1}{\pi} \int_{-\pi/2}^{\pi/2} \exp\left[\frac{\phi_1 - \phi_2}{k_{\text{B}}T}p(x, y_{\text{m}}(x), \beta_E)\right] d\breve{x}}{\cosh\frac{\phi_1 - \phi_2}{2k_{\text{B}}T}} \tag{6.19}$$

which only depends on the normalized work function difference $(\phi_1 - \phi_2)/(k_B T_i)$ and the field ratio β_E .

In the low temperature limit where the space charge effect is negligible, $-E_0 = E_{AK} = V_{AK}/d$. To estimate the effect of the space charge on the E_0 value, we made the similar assumption as Eq. 6.10 but replacing J(x) with its average value J:

$$\rho(x,y) = J\left(\frac{d}{y}\right)^{2/3} \sqrt{\frac{m}{2eV_{\text{AK}}}}$$
(6.20)

Substituting Eq. 6.20 into Eq. 6.7, we get that the electric field E_0 (or $E_y(x,0)$ in Eq. 6.7) due to the applied voltage and the space charge satisfies:

$$1 = \frac{-E_0}{E_{AK}} + \frac{J}{J_{FSCL}} = \frac{E_{patch}}{E_{AK}} \frac{1}{\beta_E} + \frac{J}{J_{TL}} \frac{J_{TL}}{J_{FSCL}}$$

$$(6.21)$$

where $\beta_E = E_{\text{patch}}/(-E_0)$.

When the value of J_{TL}/J_{FSCL} is given, we eliminate the variable β_E by solving the system of Eq. 6.19 and 6.21, so J/J_{TL} only depends on $(\phi_1 - \phi_2)/(k_BT_i)$ and E_{patch}/E_{AK} .

In particular, at the TL-FSCL intersection temperature T_i , $J_{TL}/J_{FSCL} = 1$ and the normalized

intersection emission restricted by the patch field effect $\alpha_{\rm PF}=J(T_{\rm i})/J_{\rm TL}(T_{\rm i})$ also only depends on two parameters: (1) the normalized work function difference $(\phi_1-\phi_2)/(k_{\rm B}T_{\rm i})$ and (2) the patch-diode field ratio $E_{\rm patch}/E_{\rm AK}=[(\phi_1-\phi_2)/(ea)]/(V_{\rm AK}/d)$.

6.7 Shape of Miram curve knee

We develop complementary, limiting-case analytic theory models to separately estimate the effects of space charge and patch fields on the shape of the Miram curve, finding out that there are three main physical parameters significantly affecting the shape of the knee: (1) the normalized work function difference $(\phi_1 - \phi_2)/(k_B T_i)$, (2) the patch-diode size ratio a/d, and (3) the patch-diode field ratio $E_{\text{patch}}/E_{\text{AK}} = [(\phi_1 - \phi_2)/(ea)]/(V_{\text{AK}}/d)$.

Fig. 6.4 shows the Miram curves predicted by our analytic models in different cases, compared with the simulation results using the nonuniform emission model[37] and their TL and FSCL extrapolations. The values of the three main physical parameters, the TL-FSCL intersection temperature T_i calculated using Eq. 6.2, and the normalized intersection emission α values defined in Eq. 6.6 for each case in Fig. 6.4 are listed in Table 6.1.

Table 6.1: Values of the parameters in the cases in Fig. 6.4

Subfigure	$\frac{\phi_1 - \phi_2}{k_{\rm B}T_{\rm i}}$	$\frac{a}{d}$	$\frac{E_{\mathrm{patch}}}{E_{\mathrm{AK}}}$	$T_{\rm i}\left({ m K} ight)$	α
(a)	4.01	0.00005	20	1327	0.1890
(b)	4.31	0.001	1	1327	0.5380
(c)	4.37	0.02	0.05	1327	0.9090
(d)	4.37	0.4	0.0025	1327	0.7378
(e)	0.89	0.02	0.01	1305	0.9853

In Fig. 6.4a and 6.4b, the patch fields have more significant impact than the space charge in restricting the emission current. The Miram curves predicted by our patch field limiting case theoretical model (dashed magenta curves) are consistent with simulation results (solid black curve)[37].

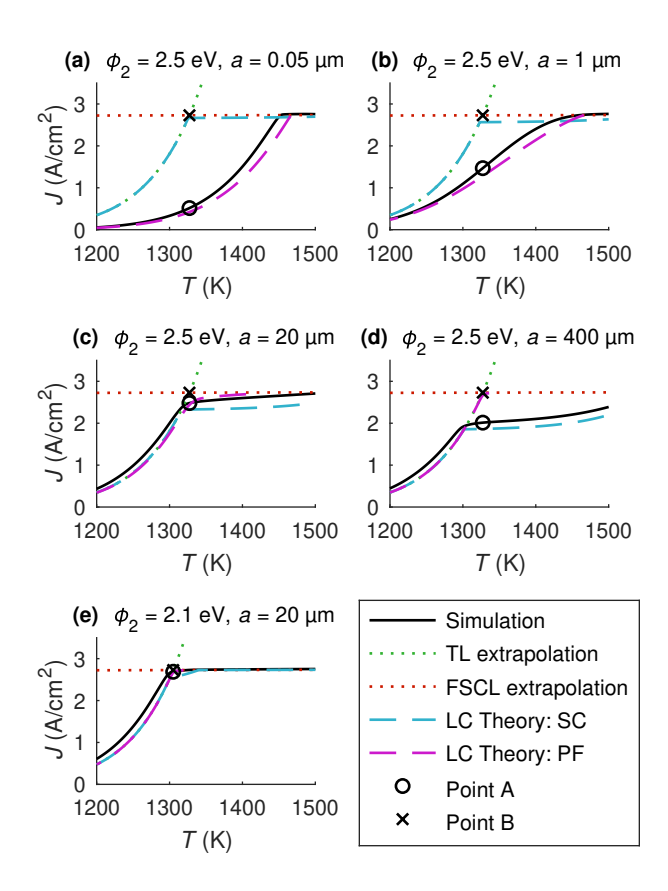


Figure 6.4: Predicted Miram curves by limiting-case (LC) theories (dashed sky-blue curve for space charge limiting case, dashed magenta curve for patch field limiting case) compared with the simulation results of nonuniform emission model (solid black curve), from a zebra crossing work function distribution, with $\phi_1 = 2 \,\text{eV}$, $d = 1 \,\text{mm}$, $V = 500 \,\text{V}$. The dotted green and red curves are the TL and FSCL extrapolation, respectively. The "o" and "×" symbols indicate the TL-FSCL intersection temperature T_i calculated using Eq. 6.2. "o" is the Point A in Fig. 6.3, while "×" is Point B. Different subfigures have different values of ϕ_2 and the stripe width a, as shown in the title of each subfigure.

When $E_{\text{patch}}/E_{\text{AK}} \gg 1$ (Fig. 6.4a), there is a significant discrepancy between the simulated Miram curve (solid black curve) and its TL extrapolation (dotted green curve, which overlaps with the dashed sky-blue space charge limiting case model curve at low temperatures). In this case, the patch field effect significantly lowers the emission current in TL region, resulting in a knee temperature much higher than the intersection temperature T_i of the TL and FSCL extrapolations (Points A and B). The normalized intersection emission α value is very low.

When $E_{\rm patch}/E_{\rm AK} \approx 1$ (Fig. 6.4b), the patch field effect moderately lowers the emission current in TL region and leads to a very rounded knee. In this case, the knee temperature is slightly higher than $T_{\rm i}$ and α is moderately low.

Fig. 6.4c is an example where the impacts of both effects are comparable and not negligible. The α value is high (close to 1).

In Fig. 6.4d, the space charge effect restricts the emission current, causing the saturated emission current density to be not flat. In this case, the simulated Miram curve is step-shaped (solid black curve), consistent with the results predicted by our limit case theoretical model of the space charge effect (dashed sky-blue curve). α is again moderately low.

The normalized work function difference $(\phi_1 - \phi_2)/(k_B T_i)$ governs the impact of both the patch field and space charge effects. Decreasing this parameter is one of the methods to lessen the restriction on the emission current due to both patch fields and space charge effects, resulting in a sharp knee at low temperature and a flat saturated emission current density (Fig. 6.4e). In this case, the α value is very high, close to 1.

6.8 Physical factors impacting normalized emission at TL-FSCL intersection temperature

As Fig. 6.4 shows, a large value of the normalized emission value α at TL-FSCL intersection temperature represents good cathode performance, indicating that neither the space charge nor the patch field effects significantly restrict the knee-temperature emission current and that the Miram curve has a sharp knee at a temperature close to T_i with a flat saturated emission current. A small α

value represents that the space charge (local to the cathode) and/or patch field effects significantly restrict the knee-temperature emission current, resulting in a rounded knee, an increased knee temperature, and/or an inclined saturated emission current.

To further illustrate the quantitative effects of the physical factors to the Miram curve knee, we plot the predicted α value as a function of the three main physical parameters in Fig. 6.5, using our theoretical studies. The lower these three parameters are, the higher the normalized intersection emission parameter α is, implying a sharper knee at a lower temperature with a flatter saturated emission current and a better cathode performance.

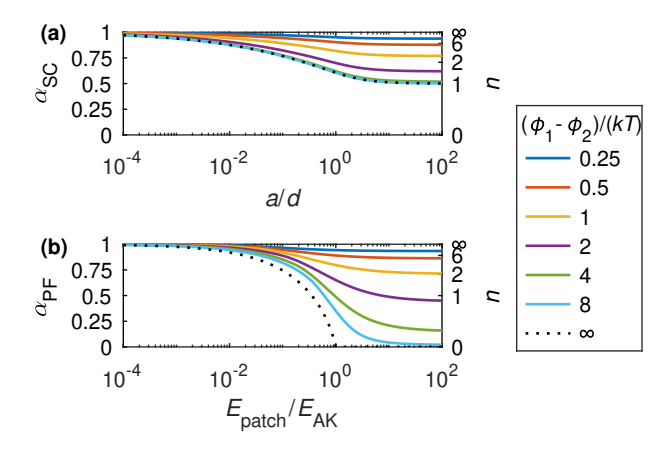


Figure 6.5: The normalized intersection emission parameter α as a function of the three main physical parameters. (a) Space-charge-restricted α_{SC} only depends on the normalized work function difference $(\phi_1 - \phi_2)/(k_B T_i)$ and the patch-diode size ratio a/d. (b) Patch-field-restricted α_{PF} only depends on the normalized work function difference $(\phi_1 - \phi_2)/(k_B T_i)$ and the patch-diode field ratio $E_{\text{patch}}/E_{AK} = [(\phi_1 - \phi_2)/(ea)]/(V_{AK}/d)$. The right vertical axis is the value of the corresponding Longo parameter n, obtained from the relationship $\alpha = 2^{-1/n}$.

Fig. 6.4a – 6.4d show the results where the values of work function, the anode-cathode distance, and the anode-cathode voltage are fixed but the patch size a is variable. Fig. 6.6 illustrates the relationship between the normalized intersection emission parameter α and patch size a. In the cases of a small patch size , a/d is small but $E_{\text{patch}}/E_{\text{AK}}$ is large, so the emission tends to be patch-field-restricted (Fig. 6.4a and 6.4b). In the cases of a large patch size,a/d is large but

 $E_{\rm patch}/E_{\rm AK}$ is small, so the emission tends to be space-charge-restricted (Fig. 6.4d). For the illustrative parameters of Fig. 6.4, the boundary between the patch-field-restricted and the space-charge-restricted regimes approximately locates at $a\approx 20\,\mu{\rm m}$ (Fig. 6.4c). This result indicates that for a zebra crossing model, when ϕ_1 , ϕ_2 , d, and V are fixed, there exists an optimal patch size a which leads to a highest normalized intersection emission α . This indicates that for a given cathode material (work function values fixed) and a given diode fixture (d and V fixed), there exists an optimal effective emission patch size so that the cathode can have the best knee performance.

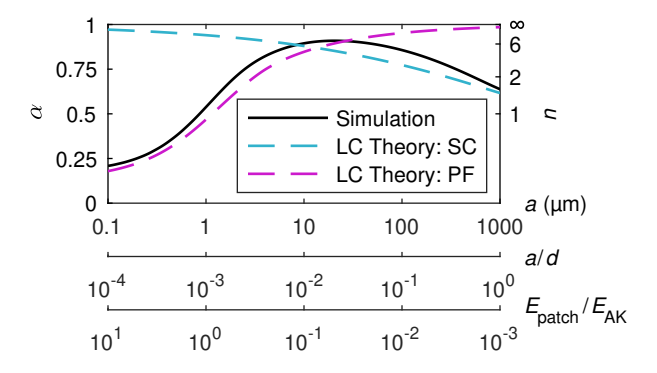


Figure 6.6: Comparison between the results of our limiting-case (LC) theoretical models (dashed sky-blue curve for theory of space charge, dashed magenta curve for patch fields) and the simulation (solid black) of zebra crossing work function distributions with $\phi_1 = 2_{\rm eV}$, $\phi_2 = 2.5_{\rm eV}$, d = 1 mm, V = 500 V, and various a values. The right vertical axis is the value of the corresponding Longo parameter n, obtained from the relationship $\alpha = 2^{-1/n}$.

6.9 Relationship to Longo-Vaughan equation

The Longo-Vaughan equation [34] $J_{\text{TL}}^{-n} + J_{\text{FSCL}}^{-n} = J^{-n}$ is a commonly used empirical equation to describe the smooth rounded knee in Miram curves. Solving the system of the Longo-Vaughan equation and Eq. 6.2, we get a relationship between the Longo-Vaughan parameter n and the normalized knee emission parameter α , i.e., $\alpha = 2^{-1/n}$. Such a relation is plotted in the vertical axis on the right in Fig. 6.5 and 6.6. Vaughan [34] pointed out that well-designed and well-made electron guns have n values in the range of 6 to 10, which corresponds to α values of 0.89 to 0.93,

while diodes with so-called "patchy emission", ascribed to uneven heating or other defects, have n in the 2 to 5 range, corresponding to α values of 0.71 to 0.87.

6.10 Summary

In this work, we used an equal-width periodic striped (zebra crossing) work function spatial distribution to study nonuniform thermionic emission. We used a normalized emission parameter α at the TL-FSCL intersection temperature to quantify the shape of the Miram curve knees. We developed complementary, limiting-case analytic models to separately estimate the effects of space charge and patch fields, and found that there are three main physical parameters which significantly affect the shape of the knee: (1) the normalized work function difference $(\phi_1 - \phi_2)/(k_B T_i)$, (2) the patch-diode size ratio a/d, and (3) the patch-diode field ratio $E_{\text{patch}}/E_{\text{AK}}$. The lower these three parameters are, the higher the α value is, implying a sharper knee at a lower temperature with a flatter saturated emission current, and a better cathode performance.

This physical knowledge directly and quantitatively connects the patch size, work function values, anode-cathode voltage and anode-cathode gap distance to the shape of the Miram curve knee, providing new understanding and a guide to the design of thermionic cathodes used as electron sources in vacuum electronic devices (VEDs).

7 Discussion on fitting work function value from J-T curve

7.1 Methods

The Richardson-Laue-Dushman equation can be rewritten as

$$\ln \frac{J}{A_{\text{theory}}T^2} = \ln \frac{A}{A_{\text{theory}}} - \frac{\phi}{k_B T}$$
(7.1)

where A_0 here is the theoretical value of the Richardson constant.

This equation provides a method to obtain A/A_{theory} and ϕ by linear fit. Fig. 7.1 shows an example on how to do the linear fit:

- 1. Convert the J-T curve data to a $\log J 1/T$ plot.
- 2. Select the data points to be fitted, and do a linear fit in the $\log J 1/T$ plot.
- 3. Use the slope to calculate the fitted work function value and the intercept to calculate the fitted Richardson constant.

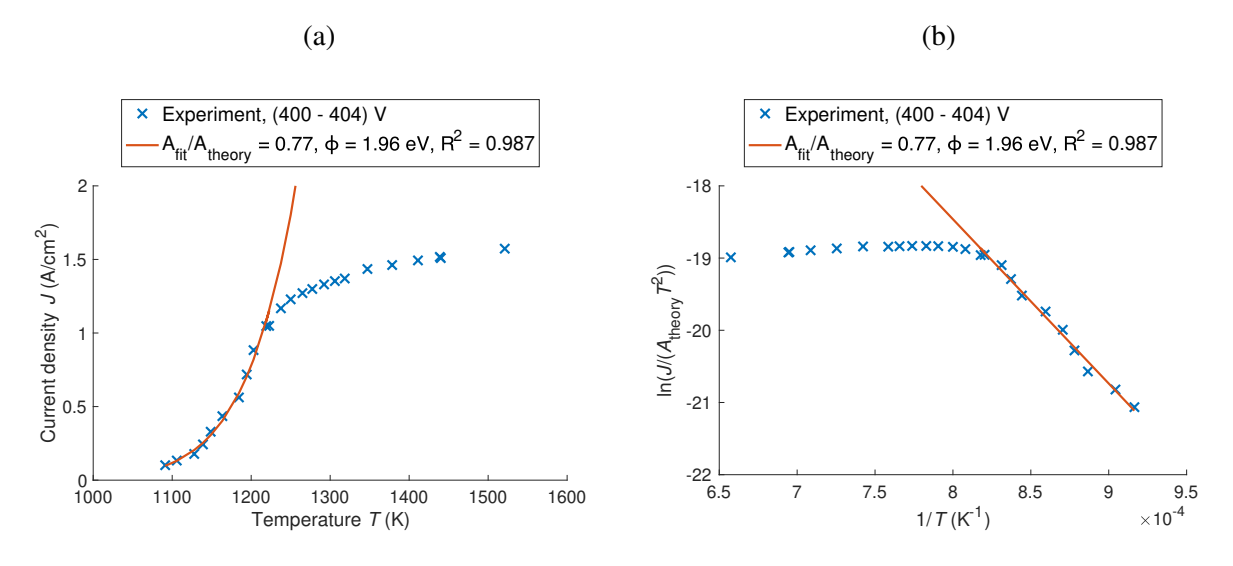


Figure 7.1: Example of fitting $A_{\rm fit}/A_{\rm theory}$ and ϕ from experimental dataset. (a) is a J-T plot. (b) is the corresponding $\log J - 1/T$ plot. Experimental data here are the same as Fig. 5.3.

It has been observed that, using this method, the fitted A values differ from the theoretical value, sometimes by many orders of magnitude, accompanied by a low ϕ value.[45] Such a low ϕ may not lead to high emission due to the accompanying small A. Thermionic cathode users usually focus on the question if a cathode can reach high emission current density at low temperature. Such a pair of a low ϕ and a small A may not necessarily lead to high emission.

7.2 Physical effects and fitted values

To study the relation between the physical effects and the fitted values of A and ϕ , I calculated the J-T curves and fit the A and ϕ for zebra crossing work function models with the parameters ranging within:

$$\phi_1 = 2 \text{ eV}$$

$$\phi_2 = 2 \text{ to } 3 \text{ eV} \ge \phi_1$$

$$a = 10^{-7} \text{ to } 10^{-3} \text{ m}$$

$$d = 10^{-3.5} \text{ to } 10^{-1.5} \text{ m}$$

$$V = 10^{1.5} \text{ to } 10^{3.5} \text{ V}$$
(7.2)

Uniformly sampling ϕ_1 , ϕ_2 , $\log a$, $\log d$, $\log V$ within the range above, Fig. 7.2a shows the relation between the fitted ϕ versus two key parameters associated with the patch field effect. It shows that small fitted ϕ values typically happens when the field ratio $E_{\text{patch}}/E_{\text{AK}} \sim 1$. Such a trend is consistent with the results from limiting-case analytic study (Fig. 7.2b).

The scatter plot of fitted ϕ value versus $A_{\rm fit}/A_{\rm theory}$ (Fig. 7.3) shows that a low fitted ϕ is accompanied by a small fitted A, and it does not lead to higher emission at the same temperature. Fig. 7.4 is an example showing an extreme case of a low fitted ϕ with an extremely small fitted A value.

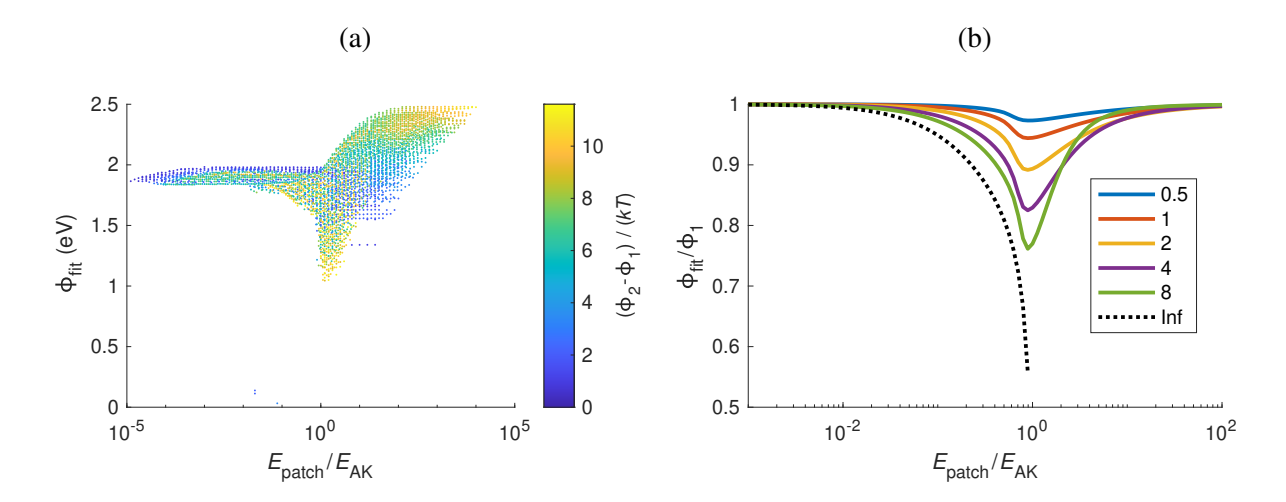


Figure 7.2: Relation between the fitted ϕ versus two key parameters associated with the patch field effect. (a) is from doing linear fit on the nonuniform emission model results on a zebra crossing work function distribution model with parameters ranging within Eq. 7.2. (b) is the results from the limiting-case analytic study.

7.3 Summary

In this work, I discuss the method of simultaneously fitting both Richardson constant A and work function ϕ from J-T data. The results show that the patch field and the space charge can cause the fitted work function value much lower than any local work function values, even if the theoretical value of the Richardson constant is used in the nonuniform emission model. In this case, such a low fitted work function value does not mean a high emission current density as it is accompanied by a small Richardson constant. This results indicate that it may be misleading to only report the fitting ϕ value without mentioning the fitted A value. A better way to report thermionic emission data is either to report the J-T curve, or the fitted value of the (A, ϕ) pair.

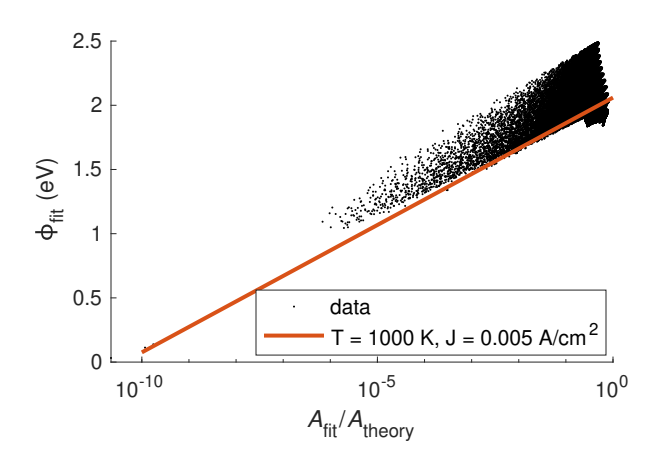


Figure 7.3: Scatter plot of fitted ϕ value versus $A_{\rm fit}/A_{\rm theory}$. Data are from doing linear fit on the nonuniform emission model results on a zebra crossing work function distribution model with parameters ranging within Eq. 7.2.

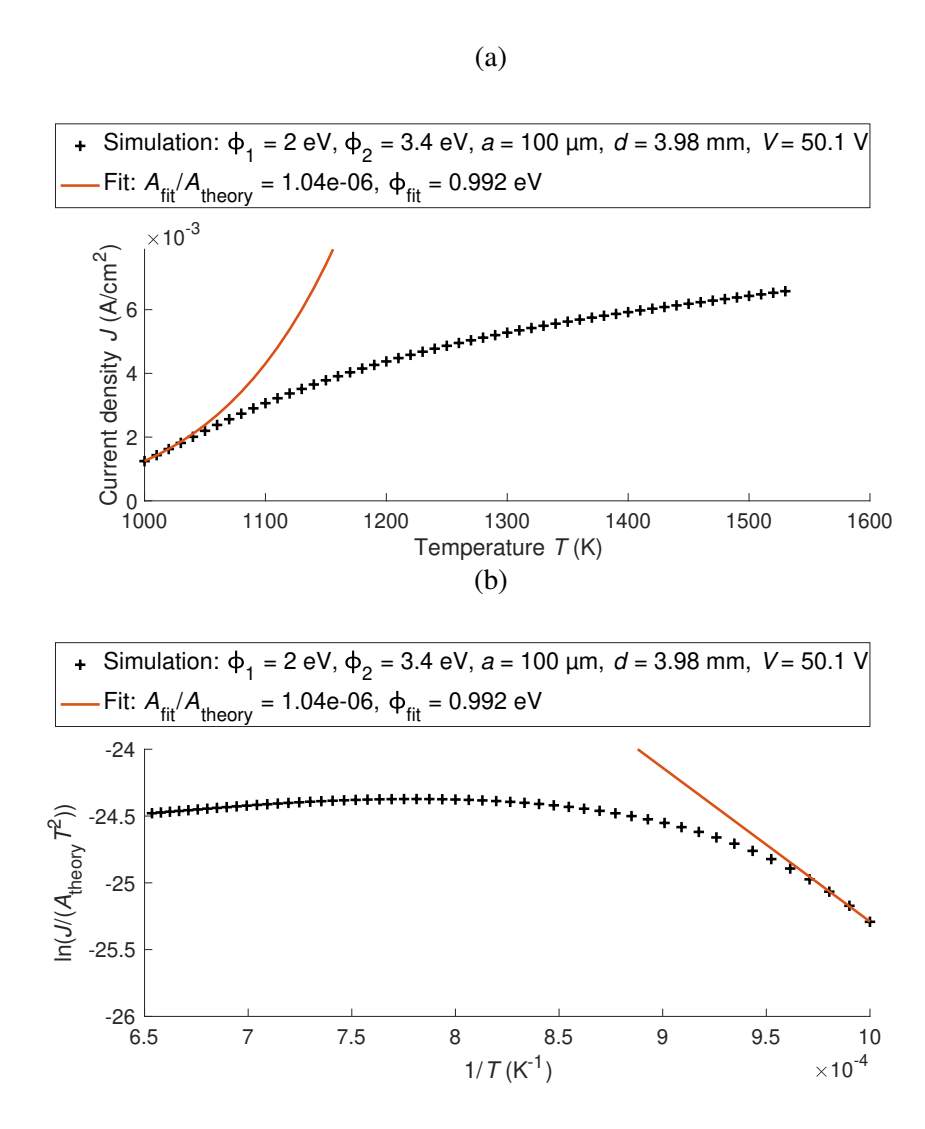


Figure 7.4: Example that the fitted work function value is lower than any local work function values. (a) is a J-T plot. (b) is the corresponding $\log J - 1/T$ plot.

8 Conclusions and outlook

8.1 Summary and impact of this work

In my PhD work, I demonstrate that the experimentally observed smooth TL-FSCL transition does not require frequently used *a priori* assumptions of a continuous distribution of work functions on the cathode surface. Instead, the smooth transition arises as a natural consequence of the physics of nonuniform thermionic emission from a spatially heterogeneous cathode surface. I obtain this smooth transition for both J-T and J-V curves using a predictive nonuniform thermionic emission model that includes 3-D space charge, patch fields (electrostatic potential nonuniformity on the cathode surface based on local work function values), and Schottky barrier lowering physics and illustrate that a smooth knee can arise from a thermionic cathode surface with as few as two discrete work function values. Importantly, I find that the inclusion of patch field effects is crucial for obtaining accurate J-T and J-V curves, and the further inclusion of Schottky barrier lowering is needed for accurate J-V curves.

As a further study, I apply this nonuniform emission model on real cathodes, by incorporating the cathode surface grain orientation via electron backscatter diffraction (EBSD) and the facetorientation-specific work function values from density functional theory (DFT) calculations. The model enables construction of two-dimensional emission current density maps of the cathode surface and corresponding J - T and J - V curves. The predicted emission curves show excellent agreement with experiment, not only in TL and FSCL regions but, crucially, also in the TL-FSCL transition region. This model provides a method to predict the thermionic emission from the microstructure of a commercial cathode, and improves the understanding on the relationship between thermionic emission and cathode microstructure.

The smooth TL-FSCL transition in a Miram curve is sometimes referred to as the "roll-off" or "Miram curve knee". The shape of the Miram curve knee is an important figure of merit for thermionic vacuum cathodes. Cathodes with a sharp Miram curve knee at a low temperature with a flat saturated emission current are typically preferred. Our previous work on modeling nonuniform

thermionic emission revealed that the space charge effect and patch field effect are critical to realizing the characteristics of the shape of Miram curve knees. This work provides a more complete understanding of the physical factors connecting these effects and their relative impact on the shape of the knee, including the smoothness, the temperature, and the flatness of the saturated emission current density. I use a periodic, equal-width striped ("zebra crossing") work function distribution as a model example, illustrating how the space charge and patch field effects restrict the emission current density near the Miram curve knee. The results indicate there are three main physical parameters which significantly impact the shape of the Miram curve. Such physical knowledge directly connects the patch size, work function values, anode-cathode voltage, and anode-cathode gap distance to the shape of the Miram curve.

I also do further studies and discussions on the method of simultaneously fitting both Richardson constant A and work function ϕ from J-T data. The results show that the patch field and the space charge can cause the fitted work function value much lower than any local work function values. In this case, such a low fitted work function value does not mean a high emission current density as it is accompanied by a small Richardson constant. This results indicate that it may be misleading to only report the fitting ϕ value without mentioning the fitted A value. I think a good way to report thermionic emission data is either to report the J-T curve, or the fitted value of the (A,ϕ) pair.

The knowledge obtained in this work demonstrate the value of the developed model in predicting the nonuniform thermionic emission from a heterogeneous cathode surface and suggests that the smooth transition behavior observed in experiments may have its origin in the nonuniform emission from relatively simple work function distributions on surfaces. The effects of space charge, patch fields, and Schottky barrier lowering have been studied separately in previous studies. However, this work has unified all of these effects and applied the resulting model to predict the emission current density as a function of temperature and applied voltage for TL and FSCL regions, and, crucially, study the impact of the nonuniformity on the transition region between TL and FSCL regions. We anticipate the emission model presented here will enable further explo-

rations and improved understanding of the interplay of surface physics properties of a cathode and the resulting engineering and design of an array of devices incorporating thermionic cathodes.

8.2 Suggestions for future directions

Although the prediction of my nonuniform emission model is consistent with experimental results for an S-type cathode, there are some assumptions in my model. Using less assumptions means the model is closer to the actual physics and is capable for more conditions.

8.2.1 Quantum effects

In my current model, I neglect the quantum tunneling and quantum reflection effects. Although these effects are negligible in thermionic emission, the quantum effects are significant in field emission. Including the quantum effects into the model makes it capable to extend my model to field emission.

8.2.2 Lateral momentum of electrons

In my current model, I neglect the lateral momentum of electrons. This assumption allows a faster method to calculate the total emission current, or equivalently, the average current density. However, without the consideration of the lateral momentum of electrons, the model is not capable to do full electron beam simulation, for example, the emittance. Therefore, it will be helpful to include the lateral momentum of electrons into the model to study the effects of nonuniform emission more thoroughly. Advanced electron optics simulation codes may be helpful for this topic.

8.2.3 Rough cathode surface

In my model, I assume the cathode surface is perfectly flat, neglecting the field enhancement effect. However, the actual surface of dispenser cathodes is rough, due to the machining and the grain structure. The field enhancement effect points out the effects of rough cathode surface with

a single work function value. Studies on the rough cathode surface with multiple work function values can help to understand the field enhancement effects when the patch field effect exists.

8.2.4 Electron beam simulation

My model is assume the diode has the simplest electron optics structure, an infinitely parallel diode. The fixture geometry of actual vacuum electronic devices is more complicated. Therefore, electron optics simulation on the electron beam is useful in actual applications. My model can be used as an input into electron beam codes or as a guideline to update electron beam codes, making it possible to predict the electron beam from thermionic cathodes with heterogeneous work function distributions.

8.2.5 Discussion on Richardson constant.

In the nonuniform emission model mentioned above, I always use the theoretical value for the Richardson constant A. However, the A value can be affected by many parameters, including the band structure, which may have significant impact to the A value. There are many experimental emission data showing A values smaller than its theoretical value. Understanding the effects on the A value can be helpful to further understand the experimental emission data.

8.2.6 Temperature-dependent work function value

In my current model, I neglect the temperature-dependence of the work function value, even when I simulate the emission current density for a real cathode. It is known that the work function of a material is temperature-dependent. Including this effect into the model can improve the prediction of J-T curves.

8.2.7 Discussion on other data analysis methods

In my PhD work, I have discussed two popular experimental data analysis methods: the Miram curve shape and fitting work function from TL data. There are many other experimental data

analysis methods popular in the community, including the practical work function distribution (PWFD). Further discussion on these data analysis methods can be helpful to understand the impact of nonuniform emission on these data analysis methods.

References

- [1] R. J. Barker, N. C. Luhmann, J. H. Booske, and G. S. Nusinovich, *Modern microwave and millimeter-wave power electronics*, 2005.
- [2] J. H. Booske, "Plasma physics and related challenges of millimeter-wave-to-terahertz and high power microwave generation," *Physics of Plasmas*, vol. 15, no. 5, p. 055502, may 2008. [Online]. Available: http://aip.scitation.org/doi/10.1063/1.2838240
- [3] J.-Y. Gao, Y.-F. Yang, X.-K. Zhang, S.-L. Li, P. Hu, and J.-S. Wang, "A review on recent progress of thermionic cathode," *Tungsten*, no. 0123456789, pp. 1–15, sep 2020. [Online]. Available: https://doi.org/10.1007/s42864-020-00059-1http://link.springer.com/10.1007/s42864-020-00059-1
- [4] D. M. Kirkwood, S. J. Gross, T. J. Balk, M. J. Beck, J. Booske, D. Busbaher, R. Jacobs, M. E. Kordesch, B. Mitsdarffer, D. Morgan, W. D. Palmer, B. Vancil, and J. E. Yater, "Frontiers in Thermionic Cathode Research," *IEEE Transactions on Electron Devices*, vol. 65, no. 6, pp. 2061–2071, jun 2018. [Online]. Available: https://ieeexplore.ieee.org/document/8331885/
- [5] J. Cronin, "Modern dispenser cathodes," *IEE Proceedings I Solid State and Electron Devices*, vol. 128, no. 1, p. 19, 1981. [Online]. Available: https://digital-library.theiet.org/content/journals/10.1049/ip-i-1.1981.0012
- [6] V. Vlahos, Y.-L. Lee, J. H. Booske, D. Morgan, L. Turek, M. Kirshner, R. Kowalczyk, and C. Wilsen, "Ab initio investigation of the surface properties of dispenser B-type and scandate thermionic emission cathodes," *Applied Physics Letters*, vol. 94, no. 18, p. 184102, may 2009. [Online]. Available: http://aip.scitation.org/doi/10.1063/1.3129193
- [7] A. Gilmour, *Klystrons, TWTs, Magnetrons, Crossed-Field Amplifiers, and Gyrotrons*. Artech House, 2011.
- [8] R. Jacobs, D. Morgan, and J. Booske, "Work function and surface stability of tungsten-based thermionic electron emission cathodes," *APL Materials*, vol. 5, no. 11, p. 116105, nov 2017. [Online]. Available: http://aip.scitation.org/doi/10.1063/1.5006029
- [9] Q. Zhou, X. Liu, T. Maxwell, B. Vancil, T. J. Balk, and M. J. Beck, "BaxScyOz on W (001), (110), and (112) in scandate cathodes: Connecting to experiment via μO and equilibrium crystal shape," *Applied Surface Science*, vol. 458, no. July, pp. 827–838, nov 2018. [Online]. Available: https://linkinghub.elsevier.com/retrieve/pii/S0169433218319573
- [10] X. Liu, Q. Zhou, T. L. Maxwell, B. K. Vancil, M. J. Beck, and T. J. Balk, "Scandate cathode surface characterization: Emission testing, elemental analysis and morphological evaluation," *Materials Characterization*, vol. 148, pp. 188–200, feb 2019. [Online]. Available: https://linkinghub.elsevier.com/retrieve/pii/S1044580318321235
- [11] J. Wang, Y. Yang, Y. Wang, W. Liu, M. Zhou, and T. Zuo, "A review on scandia doped tungsten matrix scandate cathode," *Tungsten*, vol. 1, no. 1, pp. 91–100, mar 2019. [Online]. Available: https://doi.org/10.1007/s42864-019-00007-8http://link.springer.com/10.1007/s42864-019-00007-8

- [12] J. A. Becker, "Thermionic Electron Emission and Adsorption Part I. Thermionic Emission," *Reviews of Modern Physics*, vol. 7, no. 2, pp. 95–128, apr 1935. [Online]. Available: https://link.aps.org/doi/10.1103/RevModPhys.7.95
- [13] C. Herring and M. H. Nichols, "Thermionic Emission," *Reviews of Modern Physics*, vol. 21, no. 2, pp. 185–270, apr 1949. [Online]. Available: https://link.aps.org/doi/10.1103/RevModPhys.21.185
- [14] G. A. Haas and R. E. Thomas, "Work-Function Distribution Studies of Pressed Matrix Cathodes," *Journal of Applied Physics*, vol. 38, no. 10, pp. 3969–3981, sep 1967. [Online]. Available: http://aip.scitation.org/doi/10.1063/1.1709049
- [15] D. Norman, R. A. Tuck, H. B. Skinner, P. J. Wadsworth, T. M. Gardiner, I. W. Owen, C. H. Richardson, and G. Thornton, "Surface structure of thermionic-emission cathodes," *Physical Review Letters*, vol. 58, no. 5, pp. 519–522, feb 1987. [Online]. Available: https://link.aps.org/doi/10.1103/PhysRevLett.58.519
- [16] P. Zhang, Y. S. Ang, A. L. Garner, Á. Valfells, J. W. Luginsland, and L. K. Ang, "Space-charge limited current in nanodiodes: Ballistic, collisional, and dynamical effects," p. 100902, mar 2021. [Online]. Available: https://aip.scitation.org/doi/10.1063/5.0042355
- [17] Y. Ang, S.-J. Liang, and L. Ang, "Theoretical modeling of electron emission from graphene," *MRS Bulletin*, vol. 42, no. 07, pp. 505–510, jul 2017. [Online]. Available: http://link.springer.com/10.1557/mrs.2017.141
- [18] G. Eng, "A new correction to Schottky barrier lowering in cathodes," *Journal of Applied Physics*, vol. 58, no. 11, pp. 4365–4373, dec 1985. [Online]. Available: http://aip.scitation.org/doi/10.1063/1.335526
- [19] O. W. Richardson, ""The Emission of Electricity from Hot Bodies."," *Journal of the Röntgen Society*, vol. 18, no. 72, pp. 150–150, jul 1922. [Online]. Available: http://www.birpublications.org/doi/10.1259/jrs.1922.0041
- [20] S. Dushman, "Thermionic Emission," *Reviews of Modern Physics*, vol. 2, no. 4, pp. 381–476, oct 1930. [Online]. Available: https://link.aps.org/doi/10.1103/RevModPhys.2.381
- [21] A. S. Gilmour, *Principles of Traveling Wave Tubes*, ser. Artech House radar library. Artech House, 1994.
- [22] J. Bardeen, "Theory of the Work Function. II. The Surface Double Layer," *Physical Review*, vol. 49, no. 9, pp. 653–663, may 1936. [Online]. Available: https://link.aps.org/doi/10.1103/PhysRev.49.653
- [23] W. Schottky, "Über kalte und warme Elektronenentladungen," *Zeitschrift für Physik*, vol. 14, no. 1, pp. 63–106, dec 1923. [Online]. Available: http://link.springer.com/10.1007/BF01340034
- [24] C. D. Child, "Discharge From Hot CaO," *Physical Review (Series I)*, vol. 32, no. 5, pp. 492–511, may 1911. [Online]. Available: https://link.aps.org/doi/10.1103/PhysRevSeriesI.32.492

- [25] I. Langmuir, "The Effect of Space Charge and Initial Velocities on the Potential Distribution and Thermionic Current between Parallel Plane Electrodes," *Physical Review*, vol. 21, no. 4, pp. 419–435, apr 1923. [Online]. Available: https://link.aps.org/doi/10.1103/PhysRev.21.419
- [26] T. C. Fry, "The Thermonic Current between Parallel Plane Electrodes; velocities of emission distributed according to Maxwell's Law," *Physical Review*, vol. 17, no. 4, pp. 441–452, 1921.
- [27] J. B. Scott, "Extension of Langmuir space-charge theory into the accelerating field range," *Journal of Applied Physics*, vol. 52, no. 7, pp. 4406–4410, jul 1981. [Online]. Available: http://aip.scitation.org/doi/10.1063/1.329367
- [28] J. Trigueiro, N. Bundaleski, A. G. Silva, and O. M. Teodoro, "Influence of the patch field on work function study using the onset method," *Vacuum*, vol. 98, pp. 41–44, dec 2013. [Online]. Available: https://linkinghub.elsevier.com/retrieve/pii/S0042207X13001218
- [29] T. Schultz, T. Lenz, N. Kotadiya, G. Heimel, G. Glasser, R. Berger, P. W. M. Blom, P. Amsalem, D. M. de Leeuw, and N. Koch, "Reliable Work Function Determination of Multicomponent Surfaces and Interfaces: The Role of Electrostatic Potentials in Ultraviolet Photoelectron Spectroscopy," *Advanced Materials Interfaces*, vol. 4, no. 19, p. 1700324, oct 2017. [Online]. Available: http://doi.wiley.com/10.1002/admi.201700324
- [30] L. K. Hansen, "Anomalous Schottky Effect," *Journal of Applied Physics*, vol. 37, no. 12, pp. 4498–4502, nov 1966. [Online]. Available: http://aip.scitation.org/doi/10.1063/1.1708068
- [31] D. Chernin, Y. Y. Lau, J. J. Petillo, S. Ovtchinnikov, D. Chen, A. Jassem, R. Jacobs, D. Morgan, and J. H. Booske, "Effect of Nonuniform Emission on Miram Curves," *IEEE Transactions on Plasma Science*, vol. 48, no. 1, pp. 146–155, jan 2020. [Online]. Available: https://ieeexplore.ieee.org/document/8966666/
- [32] A. Jassem, D. Chernin, J. J. Petillo, Y. Y. Lau, A. Jensen, and S. Ovtchinnikov, "Analysis of Anode Current From a Thermionic Cathode With a 2-D Work Function Distribution," *IEEE Transactions on Plasma Science*, pp. 1–7, 2021. [Online]. Available: https://ieeexplore.ieee.org/document/9332265/
- [33] R. Longo, "A study of thermionic emitters in the regime of practical operation," in *1980 International Electron Devices Meeting*. IRE, 1980, pp. 467–470. [Online]. Available: http://ieeexplore.ieee.org/document/1481311/
- [34] R. Vaughan, "A synthesis of the Longo and Eng cathode emission models," *IEEE Transactions on Electron Devices*, vol. 33, no. 11, pp. 1925–1927, nov 1986. [Online]. Available: http://ieeexplore.ieee.org/document/1486061/
- [35] M. Cattelino and G. Miram, "Predicting cathode life expectancy and emission quality from PWFD measurements," *Applied Surface Science*, vol. 111, pp. 90–95, feb 1997. [Online]. Available: https://linkinghub.elsevier.com/retrieve/pii/S0169433296007180
- [36] O. Richardson, "LI. Some applications of the electron theory of matter," *The London, Edinburgh, and Dublin Philosophical Magazine and Journal of Science*, vol. 23, no. 136,

- pp. 594–627, apr 1912. [Online]. Available: https://www.tandfonline.com/doi/full/10.1080/14786440408637250
- [37] D. Chen, R. Jacobs, D. Morgan, and J. Booske, "Impact of Nonuniform Thermionic Emission on the Transition Behavior Between Temperature-and Space-Charge-Limited Emission," *IEEE Transactions on Electron Devices*, vol. 68, no. 7, pp. 3576–3581, jul 2021. [Online]. Available: https://ieeexplore.ieee.org/document/9442892/
- [38] E. A. Adler and R. T. Longo, "Effect of nonuniform work function on space-charge-limited current," *Journal of Applied Physics*, vol. 59, no. 4, pp. 1022–1027, feb 1986. [Online]. Available: http://aip.scitation.org/doi/10.1063/1.336535
- [39] A. Sitek, K. Torfason, A. Manolescu, and Á. Valfells, "Space-Charge Effects in the Field-Assisted Thermionic Emission from Nonuniform Cathodes," *Physical Review Applied*, vol. 15, no. 1, p. 014040, jan 2021. [Online]. Available: https://doi.org/10.1103/PhysRevApplied.15.014040https://link.aps.org/doi/10.1103/PhysRevApplied.15.014040
- [40] M. J. Morant and H. House, "The Work Function and Patch Field of an Irregular Metal Surface," *Proceedings of the Physical Society. Section B*, vol. 69, no. 1, pp. 14–20, jan 1956. [Online]. Available: https://iopscience.iop.org/article/10.1088/0370-1301/69/1/303
- [41] C. E. Maloney and C. S. Fang, "Methods for evaluating the performance of emitters in plane parallel diodes," *Applied Surface Science*, vol. 24, no. 3-4, pp. 407–429, oct 1985. [Online]. Available: https://linkinghub.elsevier.com/retrieve/pii/0169433285901904
- [42] K. T. Compton and I. Langmuir, "Electrical Discharges in Gases. Part I. Survey of Fundamental Processes," *Reviews of Modern Physics*, vol. 2, no. 2, pp. 123–242, apr 1930. [Online]. Available: https://link.aps.org/doi/10.1103/RevModPhys.2.123
- [43] W. B. Nottingham, "Thermionic Emission from Tungsten and Thoriated Tungsten Filaments," *Physical Review*, vol. 49, no. 1, pp. 78–97, jan 1936. [Online]. Available: https://link.aps.org/doi/10.1103/PhysRev.49.78
- [44] Jinfeng Zhao, Na Li, Ji Li, L. R. Barnett, M. Banducci, D. Gamzina, Z. A. Munir, and N. C. Luhmann, "High Current Density and Long-Life Nanocomposite Scandate Dispenser Cathode Fabrication," *IEEE Transactions on Electron Devices*, vol. 58, no. 4, pp. 1221–1228, apr 2011. [Online]. Available: http://ieeexplore.ieee.org/document/5729802/
- [45] V. S. Fomenko, *Handbook of Thermionic Properties*, V. S. Fomenko and G. V. Samsonov, Eds. Boston, MA: Springer US, 1966. [Online]. Available: http://link.springer.com/10.1007/978-1-4684-7293-6
- [46] D. Chen, R. Jacobs, J. Petillo, V. Vlahos, K. L. Jensen, D. Morgan, and J. Booske, "Physics-based Model for Nonuniform Thermionic Electron Emission from Polycrystalline Cathodes," pp. 1–29, nov 2021. [Online]. Available: http://arxiv.org/abs/2112.02136
- [47] D. Jones, D. McNeely, and L. Swanson, "Surface and emission characterization of the impregnated dispenser cathode," *Applications of Surface Science*, vol. 2, no. 2,

- pp. 232–257, jan 1979. [Online]. Available: https://linkinghub.elsevier.com/retrieve/pii/0378596379900369
- [48] K. L. Jensen, D. W. Feldman, M. Virgo, and P. G. O'Shea, "Measurement and analysis of thermal photoemission from a dispenser cathode," *Physical Review Special Topics Accelerators and Beams*, vol. 6, no. 8, pp. 91–104, 2003.
- [49] Y. Wan, Y. Li, Q. Wang, K. Zhang, and Y. Wu, "The relationship of surface roughness and work function of pure silver by numerical modeling," *International Journal of Electrochemical Science*, vol. 7, no. 6, pp. 5204–5216, 2012.
- [50] R. Forman, "Surface studies of barium and barium oxide on tungsten and its application to understanding the mechanism of operation of an impregnated tungsten cathode," *Journal of Applied Physics*, vol. 47, no. 12, pp. 5272–5279, dec 1976. [Online]. Available: http://aip.scitation.org/doi/10.1063/1.322602
- [51] G. Haas, A. Shih, and C. Marrian, "Interatomic Auger analysis of the oxidation of thin Ba films," *Applications of Surface Science*, vol. 16, no. 1-2, pp. 139–162, may 1983. [Online]. Available: https://linkinghub.elsevier.com/retrieve/pii/0378596383900648
- [52] V. Vlahos, J. H. Booske, and D. Morgan, "Ab initio investigation of barium-scandium-oxygen coatings on tungsten for electron emitting cathodes," *Physical Review B*, vol. 81, no. 5, p. 054207, feb 2010. [Online]. Available: https://link.aps.org/doi/10.1103/PhysRevB.81.054207
- [53] M. V. Mroz, T. Savina, M. E. Kordesch, J. T. Sadowski, and S. A. Tenney, "Solid-solid dewetting of scandium thin films on the W(100) surface observed using emission microscopy," *Journal of Vacuum Science & Technology B*, vol. 37, no. 1, p. 012903, 2019. [Online]. Available: http://dx.doi.org/10.1116/1.5066015
- [54] R. A. Tuck, "Surface studies of thermionic emitters by methods unique to them," *Applications of Surface Science*, vol. 2, no. 2, pp. 128–148, jan 1979. [Online]. Available: https://linkinghub.elsevier.com/retrieve/pii/0378596379900308
- [55] C. Wan, J. M. Vaughn, J. T. Sadowski, and M. E. Kordesch, "Scandium oxide coated polycrystalline tungsten studied using emission microscopy and photoelectron spectroscopy," *Ultramicroscopy*, vol. 119, pp. 106–110, aug 2012. [Online]. Available: https://linkinghub.elsevier.com/retrieve/pii/S0304399111002385
- [56] J. M. Vaughn, K. D. Jamison, and M. E. Kordesch, "In Situ Emission Microscopy of Scandium/Scandium-Oxide and Barium/Barium-Oxide Thin Films on Tungsten," *IEEE Transactions on Electron Devices*, vol. 56, no. 5, pp. 794–798, may 2009. [Online]. Available: http://ieeexplore.ieee.org/document/4806053/
- [57] —, "17.3: Work function reduction by multilayer oxides :Thermionic electron emission microscopy of scandium oxide and barium oxide on tungsten," in 2010 IEEE International Vacuum Electronics Conference (IVEC). IEEE, may 2010, pp. 421–422. [Online]. Available: http://ieeexplore.ieee.org/document/5503437/

- [58] M. E. Kordesch and C. Wan, "Barium de-wetting and thermionic emission from Ba on W," in 2013 26th International Vacuum Nanoelectronics Conference (IVNC). IEEE, jul 2013, pp. 1–2. [Online]. Available: http://ieeexplore.ieee.org/document/6624735/
- [59] C. Wan and M. E. Kordesch, "Tungstate formation in a model scandate thermionic cathode," *Journal of Vacuum Science & Technology B, Nanotechnology and Microelectronics: Materials, Processing, Measurement, and Phenomena*, vol. 31, no. 1, p. 011210, jan 2013. [Online]. Available: http://avs.scitation.org/doi/10.1116/1.4772007
- [60] F. Ren, S.-Y. Yin, Z.-P. Lu, Y. Li, Y. Wang, S.-J. Zhang, F. Yang, and D. Wei, "Applications of deep ultraviolet laser photo-and thermal-emission electron microscope in thermal dispenser cathode research," *Acta Physica Sinica*, vol. 66, no. 18, p. 187901, 2017. [Online]. Available: http://wulixb.iphy.ac.cn/article/doi/10.7498/aps.66.187901
- [61] M. Mroz, S. Tenney, T. Savina, and M. E. Kordesch, "Thermionic emission microscopy of scandium thin film dewetting on W(100)," *AIP Advances*, vol. 8, no. 6, p. 065114, jun 2018. [Online]. Available: http://dx.doi.org/10.1063/1.5039612http://aip.scitation.org/doi/10.1063/1.5039612
- [62] J. W. Luginsland, Y. Y. Lau, and R. M. Gilgenbach, "Two-Dimensional Child-Langmuir Law," *Physical Review Letters*, vol. 77, no. 22, pp. 4668–4670, nov 1996. [Online]. Available: https://link.aps.org/doi/10.1103/PhysRevLett.77.4668
- [63] Y. Y. Lau, "Simple Theory for the Two-Dimensional Child-Langmuir Law," *Physical Review Letters*, vol. 87, no. 27, pp. 278 301–278 301–3, 2001.
- [64] R. J. Umstattd and J. W. Luginsland, "Two-Dimensional Space-Charge-Limited Emission: Beam-Edge Characteristics and Applications," *Physical Review Letters*, vol. 87, no. 14, p. 145002, sep 2001. [Online]. Available: https://link.aps.org/doi/10.1103/PhysRevLett.87. 145002
- [65] J. W. Luginsland, Y. Y. Lau, R. J. Umstattd, and J. J. Watrous, "Beyond the Child–Langmuir law: A review of recent results on multidimensional space-charge-limited flow," *Physics of Plasmas*, vol. 9, no. 5, pp. 2371–2376, may 2002. [Online]. Available: http://aip.scitation.org/doi/10.1063/1.1459453
- [66] Y.-M. QUAN and Y.-G. DING, "Generalization of the two-dimensional Child–Langmuir law for non-zero injection velocities in a planar diode," *Journal of Plasma Physics*, vol. 75, no. 1, pp. 85–90, feb 2009. [Online]. Available: https://www.cambridge.org/core/product/identifier/S0022377808007423/type/journal{_}article
- [67] A. Sitek, K. Torfason, A. Manolescu, and Á. Valfells, "Edge Effect on the Current-Temperature Characteristic of Finite-Area Thermionic Cathodes," *Physical Review Applied*, vol. 16, no. 3, p. 034043, sep 2021. [Online]. Available: https://doi.org/10.1103/PhysRevApplied.16.034043https://link.aps.org/doi/10.1103/PhysRevApplied.16.034043
- [68] J. Tonnerre, D. Brion, P. Palluel, and A. Shroff, "Evaluation of the work function distribution of impregnated cathodes," *Applications of Surface Science*, vol. 16, no. 1-2, pp. 238–249, may 1983. [Online]. Available: https://linkinghub.elsevier.com/retrieve/pii/0378596383900703

- [69] K. L. Jensen, Y. Y. Lau, and N. Jordan, "Emission nonuniformity due to profilimetry variation in thermionic cathodes," *Applied Physics Letters*, vol. 88, no. 16, p. 164105, apr 2006. [Online]. Available: http://aip.scitation.org/doi/10.1063/1.2197605
- [70] D. P. Field, "Recent advances in the application of orientation imaging," *Ultramicroscopy*, vol. 67, no. 1-4, pp. 1–9, jun 1997. [Online]. Available: https://linkinghub.elsevier.com/retrieve/pii/S0304399196001040
- [71] M. M. Nowell and S. I. Wright, "Orientation effects on indexing of electron backscatter diffraction patterns," *Ultramicroscopy*, vol. 103, no. 1, pp. 41–58, apr 2005. [Online]. Available: https://linkinghub.elsevier.com/retrieve/pii/S0304399104002128
- [72] S. I. Wright and M. M. Nowell, "EBSD Image Quality Mapping," *Microscopy and Microanalysis*, vol. 12, no. 01, pp. 72–84, feb 2006. [Online]. Available: http://www.journals.cambridge.org/abstract{_}S1431927606060090
- [73] D. Chen, R. Jacobs, V. Vlahos, D. Morvan, and J. Booske, "Statistical Model of Non-Uniform Emission/rom Polycrystalline Tungsten Cathodes," in 2019 International Vacuum Electronics Conference (IVEC). IEEE, apr 2019, pp. 1–2. [Online]. Available: https://ieeexplore.ieee.org/document/8745051/
- [74] S. De Waele, K. Lejaeghere, M. Sluydts, and S. Cottenier, "Error estimates for density-functional theory predictions of surface energy and work function," *Physical Review B*, vol. 94, no. 23, p. 235418, dec 2016. [Online]. Available: https://link.aps.org/doi/10.1103/PhysRevB.94.235418
- [75] R. Tran, X.-G. Li, J. H. Montoya, D. Winston, K. A. Persson, and S. P. Ong, "Anisotropic work function of elemental crystals," *Surface Science*, vol. 687, pp. 48–55, sep 2019. [Online]. Available: https://linkinghub.elsevier.com/retrieve/pii/S003960281930127X
- [76] R. Miller, Y. Y. Lau, and J. H. Booske, "Electric field distribution on knife-edge field emitters," *Applied Physics Letters*, vol. 91, no. 7, pp. 1–4, 2007.
- [77] —, "Schottky's conjecture on multiplication of field enhancement factors," *Journal of Applied Physics*, vol. 106, no. 10, 2009.
- [78] J. Li, H. Wang, Y. Gao, H. Yuan, K. Pan, K. Zhang, Q. Chen, T. Yan, F. Liao, J. Wang, Y. Wang, and W. Liu, "Recent Developments in Scandia-Doped Dispenser Cathodes," in 2006 IEEE International Vacuum Electronics Conference held Jointly with 2006 IEEE International Vacuum Electron Sources. IEEE, 2006, pp. 51–52. [Online]. Available: http://ieeexplore.ieee.org/document/1666179/
- [79] J. Li, H. Wang, Z. Yu, Y. Gao, Q. Chen, and K. Zhang, "Emission Mechanism of High Current Density Thermionic Cathodes," in 2007 IEEE International Vacuum Electronics Conference, vol. 2440, no. 100016. IEEE, may 2007, pp. 1–2. [Online]. Available: http://ieeexplore.ieee.org/document/4283257/

- [80] J. Petillo, K. Eppley, D. Panagos, P. Blanchard, E. Nelson, N. Dionne, J. DeFord, B. Held, L. Chernyakova, W. Krueger, S. Humphries, T. McClure, A. Mondelli, J. Burdette, M. Cattelino, R. True, K. Nguyen, and B. Levush, "The michelle three-dimensional electron gun and collector modeling tool: theory and design," *IEEE Transactions on Plasma Science*, vol. 30, no. 3, pp. 1238–1264, jun 2002. [Online]. Available: http://ieeexplore.ieee.org/document/1158363/
- [81] D. Chen, R. Jacobs, D. Morgan, and J. Booske, "Physical factors governing the shape of the Miram curve knee in thermionic emission," feb 2022. [Online]. Available: http://arxiv.org/abs/2202.08247
- [82] M. Cattelino, G. Miram, and W. Ayers, "A diagnostic technique for evaluation of cathode emission performance and defects in vehicle assembly," in *1982 International Electron Devices Meeting*. IRE, 1982, pp. 36–39. [Online]. Available: http://ieeexplore.ieee.org/document/1482739/
- [83] V. Vlahos, "Private communication," 2021.